We are IntechOpen,
the world's leading publisher of
Open Access books
Built by scientists, for scientists

6,300
Open access books available

171,000
International authors and editors

190M
Downloads

Our authors are among the

154
Countries delivered to

TOP 1%
most cited scientists

12.2%
Contributors from top 500 universities

CLARIVATE ANALYTICS
BOOK CITATION INDEX
INDEXED

WEB OF SCIENCE™

Selection of our books indexed in the Book Citation Index
in Web of Science™ Core Collection (BKCI)

Interested in publishing with us?
Contact book.department@intechopen.com

Introductory Chapter: Unique Applications of Silicon Photonics

Lakshmi Narayana Deepak Kallepalli

Additional information is available at the end of the chapter

1. Introduction

Current technological demands require two key components: miniaturization of devices and integration of multifunctional components onto a single chip offered at low cost. The continuous improvement in meeting the demands of integrated circuits has been enabled by incremental efforts of miniaturization of the transistor [1]. Moore's law states that the minimum feature size shrinks by a factor of 0.7 every 2 years [2, 3]. There has been tremendous growth in the areas of semiconductors and electronics to meet these requirements. However, the research on silicon photonics started only in the 1980s [4]. The advantage of silicon is that its properties can be tailored by doping, which makes it suitable for applications both in electronics and photonics. For useful applications, the technology also plays a major role along with the material. Here, a few applications in photonics domain have been demonstrated.

2. Silicon photonics: a brief overview

Silicon photonics is a disruptive technology, in contrast to conventional technology, as it is vast and has diverse applications. Some important applications include high-performance computing, sensors, and data centers. The photonics industry is rapidly growing to meet the semiconductor and electronics industry. One key advantage can be that of the accessible bandwidth. Most of the electronic devices are limited to GHz speeds in contrast to higher speeds accessible to optical devices. This has spurred researchers develop optical devices operated with faster speeds and at low cost. Silicon photonics is accepted as the next-generation communication systems and data interconnects as it brings the advantages of integration and

photonics-high data densities and transmission over longer distances. One potential application was of waveguides in silicon-on-insulator (SOI) wafer structures in 1985 [5, 6], which was commercialized later in 1989 by Bookham Technology Ltd. [7].

The commercialization for sensor applications began in the 1990s, with integrated gyroscopes and pressure sensors being the first prototype products. Later on, commercialization changed to wavelength-division-multiplexing (WDM) telecommunications products. Here, the low-cost integration capabilities of the platform enabling high-density chips that can perform the multiplexing of many channels of high-speed data onto a single fiber demonstrated the fundamental commercial promise of the technology. The later versions of the data communications advanced the realization of SOI-waveguide p-i-n junction modulators [6] and Ge-, SiGe-based photodetectors, and modulators [8].

3. Role of ultrafast lasers

Ultrafast lasers are known to tailor the properties of materials locally anywhere in 3D to explore salient functionalities. When ultrafast laser pulses (femto and pico) are tightly focused into a material, large peak intensities at the focal volume result in nonlinear absorption and ionization (e.g., multiphoton, tunneling, or avalanche type) guiding to an array of changes in material physical and optical properties. These include negative refractive index (RI) change, positive RI change, or simply void formation. This highly controlled modification endows fs LDW a unique two-dimensional/three-dimensional (2D/3D) microfabrication capability without the use of any phase mask or special sample preparation. Large-scale structures can be fabricated easily by placing the material on a stacked 3D translation stages and control the motion in 3D pattern. In the past, several optical components such as structures for MEMS [9], 2D and 3D gratings [10–17], optical data storage [18–22], waveguides [23–26], photonic band gap materials [27–29], and micro-fluidic structures/devices [30–34]. Ultrafast lasers have been used to change the properties (optical, electrical, chemical, and physical) of silicon toward different applications like surface-enhanced Raman scattering (SERS) for sensors, and waveguides [35, 36]. Silicon also has been tested for its wettability for diverse applications in biophotonics and tissue engineering [36]. There is a need to integrate all these optical components like sensor and waveguides onto Si wafer.

4. Conclusions

The unique combination of properties of silicon combined with photonics technology has been demonstrated in several applications in the past and current. Tailoring the properties of material (silicon) such as bandgap and properties of light such as wavelength, energy, and pulse duration are shown to be the key components in several applications. In this book, some of the key applications in the area of sensors and waveguides have been highlighted.

Author details

Lakshmi Narayana Deepak Kallepalli

Address all correspondence to: lkallepa@uottawa.ca

National Research Council Laboratory for Attosecond Science, Joint University of Ottawa,
Ottawa, Ontario, Canada

References

[1] Shin C. State-of-the-art silicon device miniaturization technology and its challenges. IEICE Electronics Express. 2014;**11**(10):1-11. DOI: 10.1587/elex.11.20142005

[2] Moore GE. Cramming more components onto integrated circuits. Proceedings of the IEEE. 1998;**86**:82. DOI: 10.1109/JPROC.1998.658762

[3] International Technology Roadmap for Semiconductors (ITRS). Available from: http://public.itrs.net

[4] Thomson D, Zilkie A, Bowers JE, Komljenovic T, Reed GT, Vivien L, Marris-Morini D, Cassan E, Virot L, Fédéli J-M. Roadmap on silicon photonics. Journal of Optics. 2016; **18**:073003

[5] Soref RA, Lorenzo JP. Single-crystal silicon: A new material for 1.3 and 1.6 &mgr;m integrated-optical components. Electronics Letters. 1985;**21**:953

[6] Reed G, Headley W, Png C. Silicon photonics: The early years. Proceedings of SPIE. 2005;**5730**:596921

[7] Rickman A. The commercialization of silicon photonics. Nature Photon. 2014;**8**:579-582

[8] Liu J, Cannon DD, Wada K, Ishikawa Y, Jongthammanurak S, Danielson DT, Michel J, Kimerling LC. Tensile strained Ge p-i-n photodetectors on Si platform for C and L band telecommunications. Applied Physics Letters. 2005;**87**:011110

[9] Juodkazis S, Yamasaki K, Marcinkevicius A, Mizeikis V, Matsuo S, Misawa H, Lippert T. Microstructuring of silica and polymethylmethacrylate glasses by femtosecond irradiation for MEMS applications. Materials Research Society Symposium Proceedings. 2002;**687**:B5-B25

[10] Higgins DA, Everett TA, Xie AF, Forman SM, Ito T. High-resolution direct-write multi-photon photolithography in poly(methyl methacrylate) films. Applied Physics Letters. 2006;**88**:184101

[11] Scully PJ, Jones D, Jaroszynski DA. Femtosecond laser irradiation of polymethylmethacrylate for refractive index gratings. Journal of Optics A: Pure and Applied Optics. 2003;**5**:S92-S96

[12]   Wochnowski C, Cheng Y, Meteva K, Sugioka K, Midorikawa K, Metev S. Femtosecond-laser induced formation of grating structures in planar polymer substrates. Journal of Optics A: Pure and Applied Optics. 2005;**7**:493-501

[13]   Baum A, Scully PJ, Basanta M, Thomas CLP, Fielden PR, Goddard NJ, Perrie W, Chalker PR. Photochemistry of refractive index structures in poly (methyl methacrylate) by femtosecond laser irradiation. Optics Letters. 2007;**32**:190-192

[14]   Baum A, Scully PJ, Perrie W, Jones D, Issac R, Jaroszynski DA. Pulse-duration dependency of femtosecond laser refractive index modification in poly (methyl methacrylate). Optics Letters. 2008;**33**:651-653

[15]   Hirono S, Kasuya M, Matsuda K, Ozeki Y, Itoh K, Mochizuki H, Watanabe W. Increasing DE by heating phase gratings formed by femtosecond laser irradiation in poly(methyl methacrylate). Applied Physics Letters. 2009;**94**:241122

[16]   Katayama S, Horiike M, Hirao K, Tsutsumi N. Structures induced by irradiation of femtosecond laser pulse in polymeric materials. Journal of Polymer Science: Polymer Physics. 2002;**40**:537-544

[17]   Katayama S, Horiike M, Hirao K, Tsutsumi N. Structure induced by irradiation of femtosecond laser pulse in dyed polymeric materials. Journal of Polymer Science: Polymer Physics. 2002;**40**:2800-2806

[18]   Glezer EN, Milosavljevic M, Huang L, Finlay RJ, Her TH, Callan JP, Mazur E. Three-dimensional optical storage inside transparent materials. Optics Letters. 1996;**21**:2023-2025

[19]   Cumpston BH, Ananthavel SP, Barlow S, Dyer DL, Ehrlich JE, Erskine LL, Heikal AA, Kuebler SM, Lee IYS, McCord-Maughon D, Qin JQ, Rockel H, Rumi M, Wu XL, Marder SR, Perry JW. Two-photon polymerization initiators for three dimensional optical data storage and microfabrication. Nature. 1999;**398**:51-54

[20]   Nie Z, Lee H, Yoo H, Lee Y, Kim Y, Lim K-S, Lee M. Multilayered optical bit memory with a high signal-to-noise ratio in fluorescent polymethylmethacrylate. Applied Physics Letters. 2009;**94**:111912

[21]   Tang H, Jiu H, Jiang B, Cai J, Xing H, Zhang Q, Huang W, Xia A. Three-dimensional optical storage recording by microexplosion in a doped PMMA polymer. Proceedings of SPIE. 2005;**5643**:258-263

[22]   Kallepalli DLN, Alshehri AM, Marquez DT, Andrzejewski L, Scaiano JC, Bhardwaj R. Ultra-high density optical data storage in common transparent plastics. Nature Scientific Reports. 2016;**6**:26163. DOI: 10.1038/srep26163

[23]   Watanabe W, Sowa S, Tamaki T, Itoh K, Nishii J. Three-dimensional waveguides fabricated in poly(methyl methacrylate) by a femtosecond laser. Japanese Journal of Applied Physics. 2006;**45**:L765-L767

[24]   Zoubir A, Lopez C, Richardson M, Richardson K. Femtosecond laser fabrication of tubular waveguides in poly (methyl methacrylate). Optics Letters. 2004;**29**:1840-1842

[25] Wang K, Klimov D, Kolber Z. Waveguide fabrication in PMMA using a modified cavity femtosecond oscillator. Proceedings of SPIE. 2007;**6766**:67660Q

[26] Ohta K, Kamata M, Obara M, Sawanobori N. Optical waveguide fabrication in new glasses and PMMA with temporally tailored ultrashort laser. Proceedings of SPIE. 2004;**5340**:172

[27] Mendonca CR, Cerami LR, Shih T, Tilghman RW, Baldacchini T, Mazur E. Femtosecond laser waveguide micromachining of PMMA films with azoaromatic chromophores. Optics Express. 2008;**16**:200-206

[28] Zhou G, Ventura MJ, Vanner MR, Gu M. Use of ultrafast-laser-driven microexplosion for fabricating three-dimensional void-based diamond-lattice photonic crystals in a solid polymer material. Optics Letters. 2004;**29**:2240-2242

[29] Straub M, Gu M. Near-infrared photonic crystals with higher-order bandgaps generated by two-photon photopolymerization. Optics Letters. 2002;**27**:1824-1826

[30] Farson DF, Choi HW, Lu C, Lee LJ. Femtosecond laser bulk micromachining of micro-fluidic channels in poly (methyl methacrylate). Journal of Laser Applications. 2006;**18**: 210-215

[31] Haiducu M, Rahbar M, Foulds IG, Johnstone RW, Sameoto D, Parameswaran M. Deep-UV patterning of commercial grade PMMA for low-cost, large-scale microfluidics. Journal of Micromechanics and Microengineering. 2008;**18**:115029-115035

[32] White YV, Parrish M, Li X, Davis LM, Hofmeister W. Femtosecond micro- and nano-machining of materials for microfluidic applications. Proceedings of SPIE. 2008;**7039**: 70390J

[33] Gómez D, Goenaga I, Lizuain I, Ozaita M. Femtosecond laser ablation for microfluidics. Optical Engineering. 2005;**44**:05110

[34] Day D, Gu M. Microchannel fabrication in PMMA based on localized heating by nano-joule high repetition rate femtosecond pulses. Optics Express. 2005;**13**:5939-5946

[35] Merlen A, Sangar A, Torchio P, Kallepalli LND, Grojo D, Utéza O, Delaporte P. Multi-wavelength enhancement of silicon Raman scattering by nanoscale laser surface abla-tion. Applied Surface Science. 2013;**284**:545-548

[36] Zorba V, Persano L, Pisignano D, Athanassiou A, Stratakis E, Cingolani R, Tzanetakis P, Fotakis C. Making silicon hydrophobic: Wettability control by two-lengthscale simul-taneous patterning with femtosecond laser irradiation. Nanotechnology. 2006;**17**(13): 3234-3238

We are IntechOpen,
the world's leading publisher of
Open Access books
Built by scientists, for scientists

6,300
Open access books available

171,000
International authors and editors

190M
Downloads

Our authors are among the

154
Countries delivered to

TOP 1%
most cited scientists

12.2%
Contributors from top 500 universities

BOOK CITATION INDEX
CLARIVATE ANALYTICS
INDEXED

WEB OF SCIENCE™

Selection of our books indexed in the Book Citation Index
in Web of Science™ Core Collection (BKCI)

Interested in publishing with us?
Contact book.department@intechopen.com

Numbers displayed above are based on latest data collected.
For more information visit www.intechopen.com

Macroporous Silicon for Gas Detection

Didac Vega and Ángel Rodríguez

Additional information is available at the end of the chapter

http://dx.doi.org/10.5772/intechopen.76439

Abstract

Macroporous silicon (MPS) has been shown to be a promising material in many areas of technical interest. In particular, MPS has been applied for electronic devices and microfluidic applications. One of the most promising features of MPS is that it enables the development of optical applications using simple and cost-effective technology, compatible with MEMS fabrication processes and suitable for mass production. This chapter describes the application of MPS structures fabricated using electrochemical etching (EE) for the detection of gases of environmental concern in the wavelength range comprising 4 μm to 15 μm, such as CO_2. Vertical-modulated MPS structures are reported, whose photonic bandgaps can be placed at different wavelengths depending on the application needs. These structures have been applied to the quantification of CO_2, and these results are summarised here. Detection is performed by the direct measure of absorption, obtaining promising results with short optical paths.

Keywords: macroporous silicon, photonic crystal, electrochemical etching, non-dispersive infrared, gas sensing

1. Introduction

Macroporous silicon (MPS) has been shown to be a versatile material with a broad spectrum of promising applications [1]. MPS was first described by Lehmann in the early 1990s [2–4] and has since attracted great interest among researchers. Of the initial works in MPS development, it is also worth mentioning those from Zhang [5], Propst [6], and Parkhutik [7]. Of particular interest is the *ordered* form of MPS. In such form, pores are etched in a silicon substrate arranged in a uniform pattern. This results in an engineered material whose dielectric constant $\varepsilon(x, y, z)$ has now a characteristic spatial distribution. Given a regular, periodic ε distribution, the propagation of an electromagnetic wave through the media is affected. In particular, with

an adequately designed pattern, it is possible to create an interference pattern giving rise to *photonic bandgaps* (PBGs) and other optical characteristics for the specific structure. Such structures are thus termed photonic crystals[1] (PCs) [8]. A PBG defines a specific frequency range and, possibly, direction in the crystal, in which an electromagnetic wave propagation is forbidden through the material [9].

Thanks to the existence of PBGs, photonic crystals have been used for advanced applications in optical communications [10], photovoltaics [11], photonics [12], light emission [13], anti-reflection/blackbody emitters [14], and gas sensing [15, 16]. Particularly, in this field, the peculiar functionalities of PCs make these structures very attractive for their use in chemical sensing: gas detection [15, 17, 18] and bio-sensing [19]. The main advantage of using PCs for these areas is their potential to design and fabricate very compact and cheap photonic devices [20, 21]. Furthermore, the possibility of integration into large-scale circuits or microelectronic fabrication processes [21, 22] opens up vast opportunities for novel devices.

In particular, in this chapter, we focus on the use of MPS PCs for the optical detection and quantification of gases. More specifically, the characteristic *absorption lines*, or bands, of a gas in the infrared—that is, the *fingerprint* of the gas—are used to quantify the presence of the gas of interest. MPS demonstrates that is a suitable material and technology to operate in the mid-infrared (MIR), and is useful for the detection of environmental concern gases, such as carbon dioxide (CO_2), methane (CH_4) or nitrogen oxides (NO_x).

2. Sensing application: gas detection

Sensor demand for everyday applications is rapidly growing. The areas of use are many and multidisciplinary [23, 24]—to name a few: environmental [25, 26], safety [27], security [25], health, transportation, and wearables. Market research shows that gas sensor segment has strong growth [24] (forecast to achieve $765 M in 2020 [23]). Furthermore, climate change concerns is making governments and other agencies push the research and deployment of *smart sensor grids* for large area monitoring [28], resulting in new opportunities for emerging technologies such as ultra-compact PC sensors.

2.1. Detection strategies: optical

Optical gas detection provides very desirable advantages over other methods. In first place, pure optical methods like spectroscopy have exceptionally fast response times to changes in mixture concentration. Furthermore, the spectroscopic optical systems are highly selective: they permit identifying a target gas by its *spectral signature* or *fingerprint*[2]. Optical systems can be made extremely sensitive, though this generally requires very long optical paths.

Traditional optical-based measuring is based on the direct measurement of optical power. One of its main drawbacks is that the equipment is large and expensive. Indeed, one has to

---

[1]Nonetheless, MPS is not the only material nor technology in which PCs can be devised and fabricated.
[2]The chemical composition of a gas compound has specific vibrational (atomic bonds; from MIR to VIS) and electronic (electron excitation; from VIS to X-Ray) resonances that result in particular absorption frequencies unique for such gas.

trade-off space for detection limit. Some applications require several centimetres or even metres of optical path to reach the required sensitivity. Furthermore, spectroscopic systems are energy limited, thus they require stable and high power light sources such as lasers or thermal radiators. Spectroscopic systems also require additional complex mechanical and electronic equipment for the signal conditioning and processing. On the other hand, non-spectroscopic optical systems impose less strict requirements on some of these aspects. However, reducing the optical path length has not found a good solution until recently with the advent of PCs.

Other optical systems exist that use alternative detection strategies. Nevertheless, these alternative systems lose some of the more desirable traits of optical detection, like response time and selectivity. Special mention has to be done with respect to *terahertz gas detection*. This technology is closely related to IR optical detection: typical working frequencies range from 0.1 to 10 THz which correspond to wavelengths from 3 mm to 30 μm [29]. At these frequencies, gas molecules have mainly vibrational resonances which are then used in the same manner as for IR optical detection: by absorption measurement. Terahertz technology has been successfully applied for the detection of air pollutants and health applications [30] and long range detection. However, terahertz technology has some serious drawbacks: the principal being the generation of terahertz waves [29].For commercial and industrial applications, *non-dispersive infrared detection* seems to be the most promising optical solution. This is discussed latter in more detail.
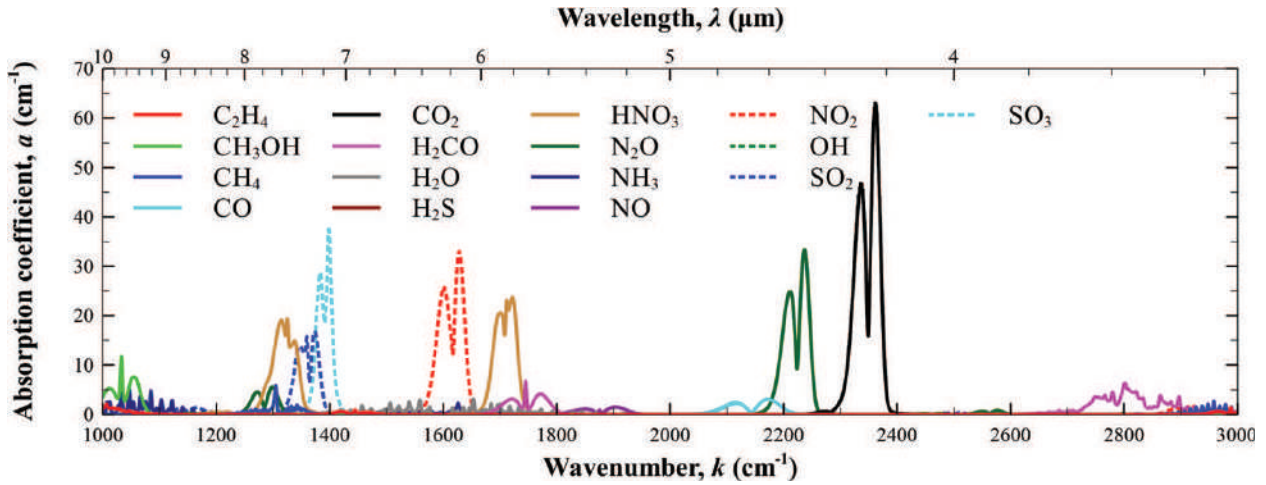
2.2. Gases of environmental concern

The growing global consciousness in environmental preservation and climate change has driven the research and development of sensing devices. In particular, monitoring the environment for pollution control [25, 31] is one of the most important applications. Gas sensors are also significant for health [32] and indoor air quality assessment [33].

Air pollutants and greenhouse gases are primarily related to the exhaust gases of combustion processes. Major air pollutants are carbon monoxide (CO), ground-level ozone (O_3), nitrogen dioxide (NO_2), and sulphur dioxide (SO_2). Greenhouse gases are carbon dioxide (CO_2), methane (CH_4), and nitrous oxide (N_2O) [34]. There are many other toxic air pollutants such as nitric oxide (NO), ammonia (NH_3), and hydrocarbons.

These gases have simple molecular composition with strong light absorption in the medium infrared wavelength range. The absorption spectrum of a gas at these light frequencies is caused by the different vibrational and rotational modes of the atomic bonds in the molecules [35]. The absorption coefficient spectra for several of the environmental concern gases are plotted in **Figure 1**. Absorption data of several gases can be found on the freely available HiTRAN database [35]. Each vibrational-rotational mode of a gas corresponds to an absorption line. These modes are narrow and close together[3]. However, at atmospheric pressure *line mixing* occurs, and the instrument resolution further broadens the spectra, transforming the absorption-lines into an *absorption region* or band, as seen in **Figure 1**.

---

[3]An ideal vibration-rotation mode has a single frequency. However, the actual *line profile* of a mode depends on external factors such as the gas pressure, velocity, temperature, etc. Typical line profiles are Gaussian (Doppler broadening), Lorentzian (pressure broadening), and Voigt (mixture of the previous). In standard conditions, ideal gas line profile separation is around $\Delta k = 2$ cm^{-1}, and full-width half-maximum approximately FWHM $= 0.2$ cm^{-1}.

Figure 1. Absorption coefficients of some of the most relevant health and environmental concern gases. The coefficients are calculated from HiTRAN data using an *apparatus function* of $\text{sinc}^2(x)$ with an aperture resolution $\Delta f = 4\ \text{cm}^{-1}$.

From the data shown in **Figure 1**, it is clear that CO_2 is potentially the largest contributor to greenhouse effect. In addition, its absorption band is clearly separated from other strong absorbers, making this gas easy to detect and quantify in an unknown mixture.

2.3. Non-dispersive infrared detection of gases

Non-dispersive infrared (NDIR) detection relies on the fact that certain absorption lines of gases are "isolated" and their wavelengths have little overlap with other gases, as seen in **Figure 1**. This is profited to simplify the design of a gas detector reducing cost, complexity, space requirements, and power [36]. Identification and quantification of a certain gas can be done looking at a narrowband region of the spectrum. This can be done using optical filters or selective light sources, or a combination. At the other end, the detector (a photodiode: PD) will give a measure of the optical power received, directly corresponding to the concentration of the gas. When light passes through a gas mixture, some wavelengths will be absorbed following the Beer–Lambert (B-L) law

$$I(\lambda) = I_0(\lambda)e^{-lca(\lambda)} \tag{1}$$

where I_0 is the optical intensity of the source (or the reference value), I is the received optical power, l is the optical path, c is the gas concentration, and a is the absorption coefficient of the gas; source intensity and absorption coefficient depend on wavelength λ. An optical filter thus selects the absorption lines to measure. This allows for a multigas detection scheme using different filters for each gas [37]. Alternatively, the absorption can be measured as follows: $A = 1 - T = 1 - I/I_0$ (where A is the absorption, and T the transmission). This is valid under the assumption that no light reflection occurs at the gas interfaces[4].

---

[4]The construction of a gas cell as well as other optical elements existing in the light path introduces several reflections. However, all of them are accounted when measuring the reference value I_0.
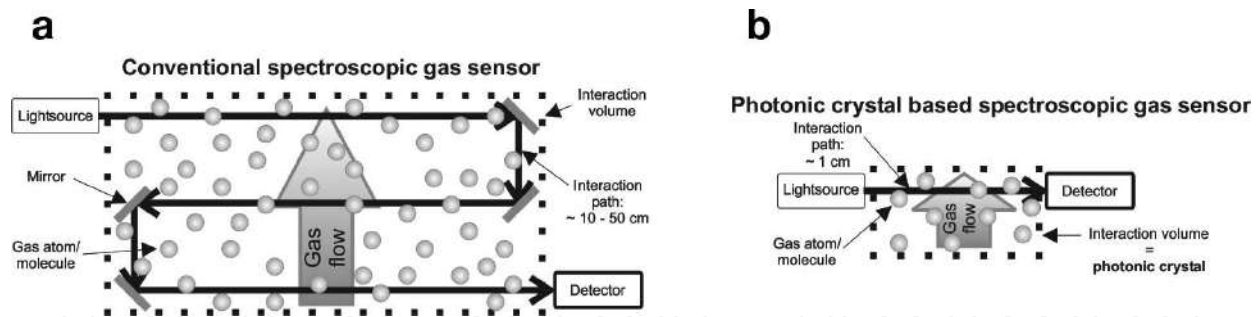
Figure 2. Conventional optical gas sensor using mirrors to attain a long optical path. A PC-based gas sensor can be made much more compact exploiting the special properties of PCs such as slow light. Reprinted from [18], with permission of SPIE.

The simplest NDIR system is depicted in **Figure 2a**. A sample of the unknown gas mixture is placed in a gas cell. Light is then passed through the cell from a source to a detector. From Eq. (1), it is clear that optical path length l is critical for the performance of the system. The necessary optical length l to achieve a desired detection limit can be several meters. Such long paths are highly impractical. Typical commercial products employ special cells (e.g., a Harriot cell) or optical systems using several mirrors to extend the effective optical path keeping a small volume.

To remedy the need of complex, bulky, and fragile optical systems to achieve the long optical paths required, a PC can be used as proposed in **Figure 2b**. PCs-based sensors are projected to require very small footprints, a few centimetres at most. The idea is to take advantage of the special features that PCs exhibit. One of such is the existence of propagation modes with extremely slow group velocity v_g (also called *slow light* modes,) such that interaction time of the propagating electromagnetic wave is increased. Another possibility is the inclusion of defects in the PC to create resonant states. These are localised [38, 39] and can have very high-quality factors (*Q*-factor) prolonging the interaction time of light with the gas. Other alternative sensing methods can be used where PCs can enhance the system response, e.g., photothermal [40, 41] or refractive index change. On the other hand, PCs can be simply used as highly selective filters.

3. Macroporous silicon applied to gas detection

Macroporous silicon is a *structured* material which has some very desirable properties. In particular, MPS has been extensively applied for the fabrication of PCs. In the first place, silicon is widely used in the industry, and many techniques and tooling exist. Additionally, MPS can benefit of established fabrication processes such as those used for micro electro-mechanical systems (MEMS). For dedicated applications, there are available fabrication technologies suitable for mass production, like electrochemical etching (EE). Given these advantageous traits, MPS has been proposed as a revolutionary material in many application areas. One of such areas is gas sensing. There has been some very intense work in order to develop the technology of MPS as gas sensing devices or as enhancers.

3.1. Seminal works

One of the first uses of MPS for gas sensing is in the work by Geppert [18]. From the analysis of the photonic band structure[5] of the PCs, they observe that some bands are very flat at certain wave vectors, thus the group velocity v_g reduces to values about $0.02c$ to $0.05c$ (c, the speed of light). The slow propagating light has more time to interact with the media making possible to reduce the physical path length while maintaining an acceptable interaction time. It is also observed that some bands have the maximum field intensity located in the high dielectric region (*dielectric bands*), while other bands have the maximum in the low ε region (*air bands*). Thus, air bands must be used for the maximum interaction.

Some of the described devices are three-dimensional (3-d) PCs made of MPS. For these devices, light is shone normal to the surface, propagating parallel to the pores' axis. The devices were used to detect ammonia (NH_3) and sulphur hexafluoride (SF_6). Transmitted light was measured through the PC and a small cavity of 300 μm depth filled with gas. They show promising results, but they argue that the small figures obtained are due to the low coupling efficiency of the PC. Furthermore, no enhancement was observed by the presence of the PC. This is also attributed to the large change in the effective refractive index[6] (n_{eff}) as for high contrast materials the transmittance $T \approx 1/n_{eff}$, thus reducing the coupling efficiency. In [18], it is also discussed a simple way to compensate for deviations in the bandgap due to fabrication tolerances: tilting the sample $15°$, a shift as large as 35 cm^{-1} of the PBG (about 4%) can be achieved.

They also present an alternative structure, refined in later works [17, 42], which uses two-dimensional (2-d) MPS structures. These are easier to fabricate and tolerances are better. As the structure is two-dimensional, the photonic band structure exists only for *in-plane* propagation. Thus, light must be coupled to the *side* of the PC. An example of such arrangement is shown in **Figure 3a**. Additionally, small v_g implies large n_{eff}, diminishing coupling efficiency. To avoid this problem, a special *tapered* section is placed on the interfaces of the PC. This tapered section gradually adapts the air n_{air} to the n_{eff} of the mode. This section can be done by deforming the lattice (elongating one axis) [18] or by leaving additional bulk material at the interfaces (promoting surface waves) [17]. The measurement results of these samples, see **Figure 3b**, show that in this case the PC does enhance moderately the detection of CO_2 (assumed 0 to 100% change). The devices have a 15 dB/mm *insertion loss*, and variability in the enhancement factor is high. These are attributed to uncertainties during fabrication: a fluctuation of 1% of the pore diameter is reported.

3.2. Structure design

From the possible strategies when using MPS structures as gas sensors, 2-d crystals impose the need to inject the light from the sides. In this way is easy to obtain long optical paths along the

---

[5]The band structure is the reciprocal of the dispersion diagram, thus the slope of the band represents the group velocity $\mathbf{v}_g = \partial\omega/\partial\mathbf{k}$, where ω is the wave frequency and $\mathbf{k}$ the wave vector in the reciprocal lattice of the PC, for a plane wave propagating through the media [62].

[6]There exist several methods to find the effective refractive index of a PC. The simplest one for low frequencies is calculating the average of the different materials that compose the PC. To obtain the n_{eff} at higher frequencies, a theoretical study of the photonic band structure is needed, from it, n_{eff} can be derived from the group velocity.
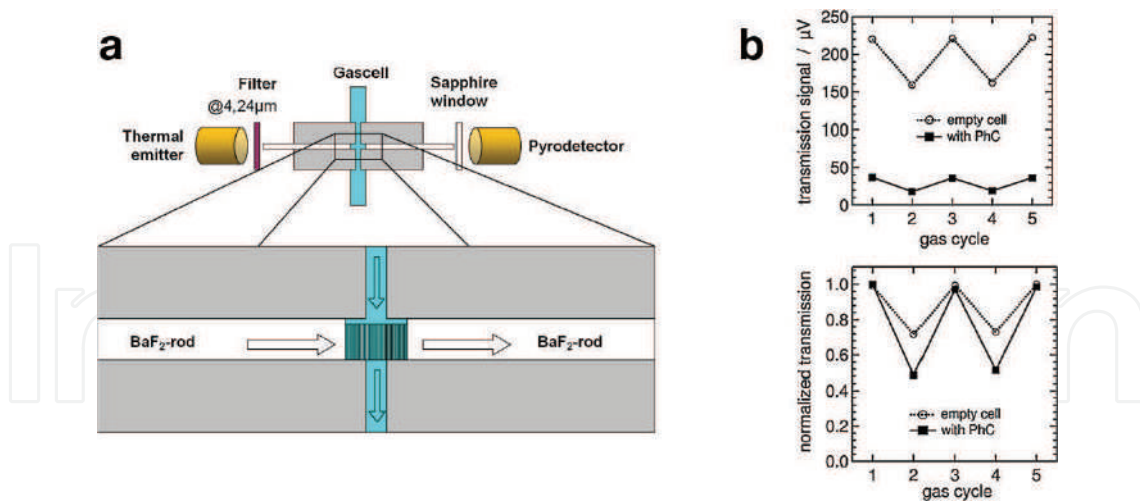
Figure 3. Optical setup for the measurement of gas using 2-d a MPS PC (a). (b) Shows results of measurement of CO_2. The top panel shows the absolute values, while the lower panel shows the relative variation of the measured value. Cycles 2 and 4 correspond to the presence of CO_2, while the other cycles are with reference atmosphere. Reprinted from [17], with the permission of AIP Publishing.

samples, but light coupling is complicated. However, from a practical standpoint, a system based on the normal incidence on the sample, using 3-d PCs, is easier to assemble, align, and calibrate[7]. In this chapter we expose results based in this option with PCs produced with macroporous silicon.

The designed MPS silicon structures are simulated using a simplified model by the finite-difference time-domain (FDTD) numerical method. Some MPS structures will be used as reflectors, while others will be used as filters. Reflection design requires a PBG encompassing just the absorption region of the desired gas. On the other hand, transmission design needs a PGB as wide as possible, with some crystal defects to block all light but the corresponding to the gas absorption line. The largest PBGs are obtained with an opal like PC [43]. As the samples will be illuminated from the top[8], the horizontal pore arrangement is not as important. Our samples pore disposition is a square array. The EE of silicon does not allow getting perfect spherical shapes (opals), but the actual pore profile has a sinusoidal-like shape, or *skewed* sinusoidal shape as seen in **Figure 4**. For the simulations, this profile is approximated by a cylinder and an ellipsoid, or by cylindrical slices, see **Figure 4**.

To place the PBG at the CO_2 absorption line, the vertical period is calculated to be around 700 nm. As a rule of thumb, in a silicon PC, optical bandgaps can be found at about four times the pitch. Therefore, to have a PBG at $\lambda_0 = 4.25$ μm, $l_0 \approx 1.1$ μm. Considering the MPS porosity[9] $\overline{p}$ is about 40%, the effective refractive index $n_{\text{eff}} = n_{\text{Si}}\overline{p} = 1.48$ [44], where $n_{\text{Si}} = 3.47$ [45]. This gives that the vertical period has to be $l_{\text{Si}} = l_0/n_{\text{eff}} = 718.0$ nm.

---

[7]Indeed, using 3-d PCs, the light can be launched into free space and coupled into the crystal from the top or bottom surface, which are much larger than the sides of the MPS structure.

[8]Concretely, the "top" surface is the surface from where the pores are etched. This surface has the initial pattern of the pore sites. For prime quality wafers, this face is polished and the incident light will have little scattering.

[9]Porosity is defined as the ratio of air to silicon volume in the unit-cell.
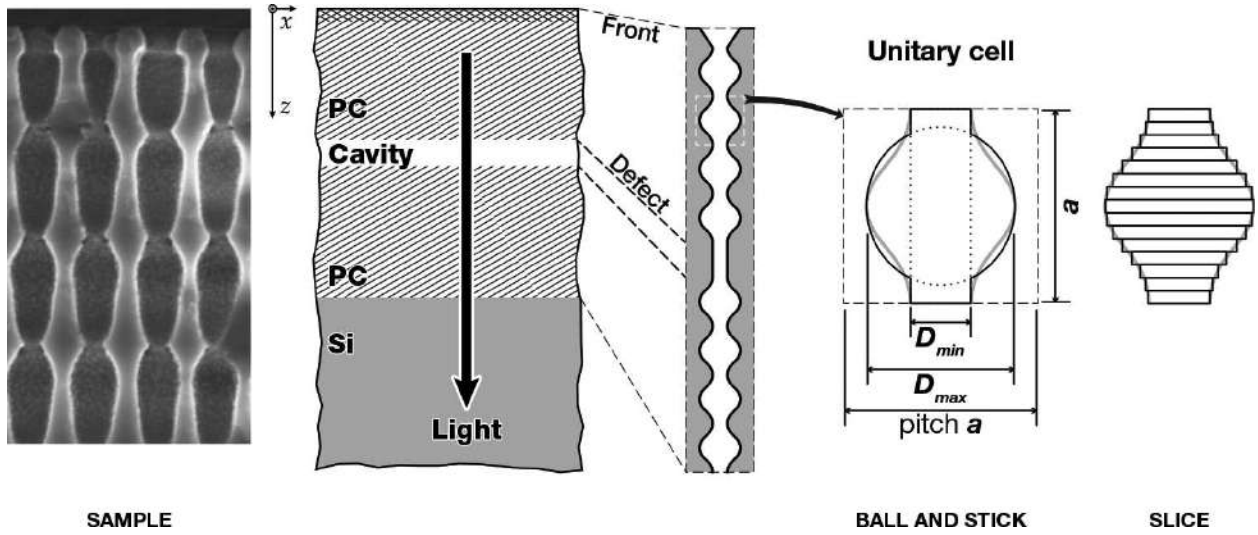
Figure 4. Sample model. The unitary cell can be approximated by a "ball and stick" model consisting of a cylinder and an ellipsoid, or by a slice method, using short cylinders.

The FDTD simulations show that in the vertical direction there is a narrow PBG (7.1%). A *chirped* modulation smoothly varying the vertical period can double the PBG width [46]. For the samples with included defects, initially the photonic response for a single defect was studied. As a further step, the use of several defects has also been analysed. In particular, the coupling between resonant cavities creates additional resonance modes [47]. Using two cavities, the fundamental resonant mode splits into two, making it possible to filter two separate frequencies using a simple PC design, to perform a differential measurement. One of the resonances selects the gas absorption line, while the other is placed in a "safe" wavelength were it will not be influenced by the media. Such configuration would allow ultra-compact filters or selective emitters.

3.3. Fabrication

For MPS fabrication, the EE method is one of the most versatile, and one of the preferred for three-dimensional structure definition. A general description of the method is the dissolution of silicon by an electrically promoted reduction–oxidation chemical process (*redox reaction*). The particular implementation of EE used for the fabrication of *ordered* MPS uses a pre-treatment of the silicon substrate to define the sites (*nucleation points*) where localised etching of the material occurs. This method was first described by Lehmann in the early 1990s [3, 4]. Succinctly, the silicon substrate to be processed is placed in a bath of hydrofluoric acid (HF). Silicon is unreactive in normal conditions with HF; however, passing a current activates the redox reaction [48]. As detailed in previous works, the reaction exchanges *holes* at the semi-conductor-HF interface. Either n-type or p-type doped silicon substrates can be used; however, for the controlled growth of macro-pores[10], n-type substrates are advantageous, as holes are

---

[10]A porous media is termed microporous for pore diameters less than 5 nm, mesoporous for 50 nm $> d_{pore} >$ 5 nm, and macroporous if pores are larger than 50 nm wide.

minority carriers. To etch the substrate holes must then be generated somehow. The most common way is by using *photogeneration* (light assisted EE). This provides great control on the etching process.

The etching setup places the patterned face to be etched in contact with the electrolyte, opposing to the cathode. The back-face (i.e., the other side) is contacted electrically to close the electrochemical circuit. The illumination can be provided from either the front or back surfaces. For practicality reasons, it is simplest to irradiate from the backside. Our etching setup follows these principles, plus the IR light is provided by IR LEDS with $\lambda_{LED} = 950$ nm, and HF is continuously pumped through the etching cell at a controlled temperature.

The pore growth and morphology depend on several factors of the etching process. The pore front (i.e., the *tip* of the pores) advances at a speed (etching velocity) relatively unaffected by the electrical conditions; however, the etch rate (i.e., the amount of dissolved silicon) is proportional to the electrical current flowing through the electrochemical cell. Thanks to this behaviour, it is possible to use the EE method to fabricate 3-d MPS structures by the modulation of the current and potential during the etching process [49]. More detailed information on the etching process can be found in the works of Lehmann [2], Zhang [5], and Kolasinski [48].

The MPS photonic crystals developed in this work have all been fabricated using the light assisted EE of silicon using n-type substrates. Having pores arranged in an *ordered* fashion generates internal interference patterns for an electromagnetic wave propagating through the porosified media. These interference patterns will depend on the direction of propagation and frequency; hence, the materialisation of a PC. To arrange the pores in a desired pattern, the method by Lehmann [4] is used. This method prepares the wafers before etching using lithography to define the pore sites. Then nucleation points are created by a short silicon anisotropic etching at the sites. This creates small pyramidal pits in the surface, which promote the electrochemical etching at these spots. EE also allows the formation of very large aspect-ratio (AR, ratio of pore diameter to pore length) pores in relatively short time. For example, AR = 1 : 465 has been reported [12].

After the porosification, some samples were post-processed to create a membrane. The membrane is done by anisotropic etching of the back face. For gas measurements, an open membrane is the best option: gas can flow freely through the MPS sample, solving any issues with gas trapping or residence time for the sensors.

3.3.1. Fabrication quality

In general, the EE of silicon produces good quality porous silicon. What is "good quality" with respect to MPS? In a minimal sense, macroporous silicon is of "good quality" if pores are of the same shape and have grown uniformly. Of course this does not provide much information whether the "quality" is acceptable for the intended application. In particular, for photonic applications, the requirements can be very strict. Fabrication imperfections arise due to numerous reasons: wafer crystalline defects, crystal alignment, and local dopant distribution; but also the etching process itself can account for some variability, and lithography errors will also cause flaws in the grown pores. The common fabrication defects one can encounter in a MPS structure fabricated by EE are summarised in **Table 1**.

Large optical influence	Little optical influence
Pore death	Spiking
Pore branching	Unstable growth
Axis alignment	Microporous layer
Cross-section	
Profile fidelity	

Table 1. Defects found in macroporous silicon.

From **Table 1**, the defects that are of greater concern are the ones classified as "large optical influence." Here *surface roughness* is not considering as a defect. It is a consequence of minute variations inherent in any fabrication process. The amount of perturbation does not alter the pore morphology or cause long-range effects and will not give unexpected results.

Pore death is the premature ending of a pore resulting in a shortened pore with respect to its neighbours. This can be single, isolated pores or can affect several pores. *Current starvation* is the most common cause. During etching, there is a minimal current under which there are not enough carriers to sustain stable growth. In this situation, current will concentrate on some pores resulting in wider, distorted, and shorter pores. The solution is increasing the etching current. Also, shorter structures are less susceptible to suffer from pore death.

Pore branching is generally a consequence of pore death but can also happen if the etching parameters are not adequate: if applied potential is too small, the space charge region (SCR) will be small and unintended holes could find their way to spots in the pore wall far from the pore tip and secondary pores grow from that points.

Pore axis alignment depends on the crystalline direction of the Si substrate. Pores preferentially develop following the principal crystalline directions of the silicon substrate; however, the pores also have a tendency to grow following the current paths. If the crystal is severely misaligned, the mismatch between the crystal direction and the current direction will cause that the pores grow in several directions simultaneously [50]. The pore *cross-section* affects the symmetry of the PC. In the stable growth phase, cross-section approximates a circle; however, under certain condition of applied potential and electrolyte additives, the cross section can change its shape.

Spiking is the appearance of random streaks of nanometric branches, spreading out in random directions and with irregular shape. Excessive voltage during the etching promotes spiking. Moderate to low spiking has little influence on the optical performance. However, it changes the porosity, which may shift the wavelengths of the optical features. *Unstable growth* is basically caused by substrate inhomogeneity, though the dynamic behaviour of the etching system may also influence [51]. In general, unstable growth is mild and can be observed with pores not evolving in a straight line but slightly wandering. Another form of unstable growth is the *long-range* variation of pore diameter.

Profile fidelity refers to the closeness of the actual pore profile to the intended profile. It is considered a defect because it is an unintended result which affects *severely* the optical response of the etched sample. Several test runs with progressive refinements are needed before the near-optimal conditions and waveforms are found. After EE, the pore's walls may be covered with a layer of *microporous silicon*. This layer will depend on the electrolyte concentration and present additives. It has no noticeable optical influence in the MIR, and it can be left; however, it is very easy to remove by a quick dip in HF.

The abovementioned discussion was made considering the local effect of perturbations in the pore shape and outcome of the etching process. Nonetheless, the uncertainties of etching, the inhomogeneity of the substrate, and the flaws in lithography can be considered on a larger scale or *long-range*. Pores at distant locations[11] are also affected by the etching system. The most common long-range effect is the variation of pore diameter of up to a few percent [42]. Also, the etching process generates H_2 bubbles which must be removed otherwise they adhere to the surface and create *big* spots where the etching stops. More in-depth analysis can be found in the works by Föll and co-workers [52, 53].

3.4. Absorption and losses of macroporous silicon

One important concern is determining how absorption and fabrication tolerances will affect the performance of the detection system. Intrinsic silicon absorbs light at wavelengths shorter than 950 nm, approximately, however when silicon is doped with impurities, strong absorption may be observed in the MIR range. Several papers report on the absorption dependence with doping level in silicon [54]. Interestingly, for the doping concentrations used in the fabrication of optical gas sensors working in the middle infrared ($n < 5 \cdot 10^{17}$ cm^{-3}), it is found that material absorption is negligible [54, 55].

On the other hand, fabrication tolerances definitively do have an impact on optical performance. For instance, in [17], it is reported that a 1% variation of the pore radius attenuates 15 dB/cm the transmitted light. This is further studied in [42], global pore diameter fluctuation of 3.5% was caused by the spatial variation of dopant. They further claim that, for a better than 90% transmission in a 1 mm thick PC, the pore position should change less than 0.3% and diameter has to be within 0.5%. A systematic study of the effect of in-plane disturbances in electrochemically etched MPS is presented in [56]. Some interesting conclusions extracted from this work are that ellipsoid perturbation up to ±10% has little impact on the PBG if the porosity is maintained near its optimum, and that a small variation of the air fraction of just ±4% is enough to shift a narrow PBG ($\Delta f = 5\%$) out of the designed central gap frequency f_0. Similar conclusion was found in the work by our group [57], where the effect of vertical period variation in 3-d MPS was analysed. Wide PBGs were designed for the samples used in this work, but noticeable narrowing and shift could be observed with periodicity variations above

---

[11] For example, a scratch on the back-surface or shadow of the illumination will cause the shape of such scratch or shadow to be transferred to the pores grown at the front surface: the affected area will have smaller diameter pores or, in extreme cases, dead pores and branching.

$\pm 5\%$. Furthermore, it was found that the PBG became more transparent allowing light transmission higher than a 10% in the forbidden band.

4. Measurements and results

Samples of MPs photonic crystals were fabricated with a lattice pitch of 700 nm and modulated pore profile. The fabrication conditions were the ones described earlier in Section 3.3—using the EE method. The modulation profiles for the 3-d PCs were programmed to generate a "strong"[12] profile having a 700 nm vertical period, the same as the lattice pitch. The samples were initially characterised to obtain their optical spectrum in the MIR range using a Vertex 70 Fourier-Transform Infrared Spectrometer (FT-IR) from Bruker Optics. Also some of the structures were cleaved and latter inspected by SEM to determine the pore morphology and actual etched profile. After the samples were analysed, the valid samples were used in a dedicated gas measuring system also using FT-IR spectrometers to measure the performance of the PCs in sensing carbon dioxide.

4.1. Fabrication, sample characterisation, and morphological study

The fabricated samples were etched using a silicon substrate with $\langle 001 \rangle$ crystal orientation. For the 700 nm period MPS structures, substrates of the appropriate resistivity were used. The pores are arranged in a square pattern. This pattern is transferred to the substrate surface using nano-imprint lithography (NIL). The etching temperature was set to $10^{\circ}C$. The resulting PCs are to be used with light coming from the top, aligned to the pores' axis, with normal or quasi-normal angle of incidence (θ_i from 0° to 13°). The actual modulation waveforms depend whether the samples will be used for reflectance or transmittance. For the samples used in transmission gas measurements, membranes were made. However, the structure resilience is critical given the thin porous layer, so membranes are *not* open. Indeed, the porosified depth of the MPS crystals ranges from 20 to 50 μm. Such thin layers are very fragile. For this reason, membranes did not reach the pore tips.

4.1.1. Morphological analysis

The morphological analysis of some samples shows, as seen in **Figure 5**, that the etched profiles of the MPS structures have some imperfections. The observed flaws are mainly small variations in pore radius between adjacent pores, pore "wiggling", skew, and pore death. On the surface of the pores, a rough finish due to microporous silicon can be appreciated (see **Figure 5**). Pore radius variation is small—less than 10%—for the samples used here. This has a small impact on the optical response of the PC as has demonstrated by our works [57] and others [58, 59]. Skew is generally not an issue. Some extreme cases have shown up to 5° of crystal misalignment from the [001] direction (see **Figure 5b**), but otherwise pores grow fine. Some pore "wiggling" can be observed in the fabricated samples (see **Figure 5a**). As a

_____

[12]This profile tries to obtain a spherical shape as close as possible.
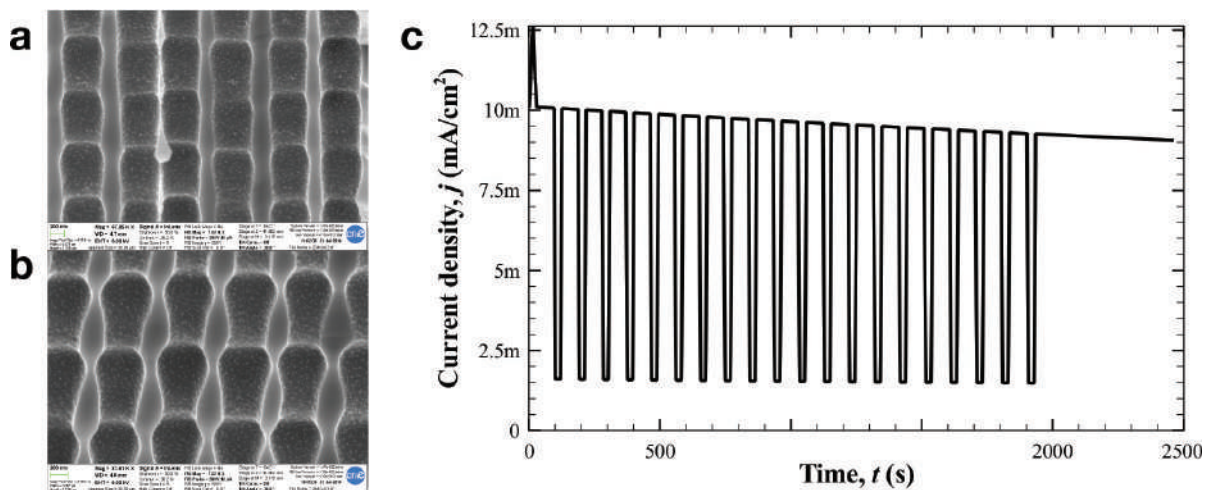
Figure 5. Cross section detail of a MPS photonic crystal (a) and (b), and the current waveform used to generate (a).

consequence, there is some decrease of the optical performance of the PC. In general, the degree of wiggling in our samples is small.

The fabrication process for the MPS samples has been optimised to obtain structures virtually free from dead pores. In general, optical performance is preserved if dead pores are few, or if pores die late during etching. To avoid pore death in the initial samples, the lower current limit was increased, so dynamic range was reduced and modulation could not be as strong as desired (compare **Figure 5a** and **b**).

The most significant defect found in the samples here used was vertical period variation[13]. As seen from **Figure 5**, for neighbouring pores, the beginning and ending of each vertical period is slightly different. As shown in our previous work [57], this variation has a noticeable influence on the PC optical response. In general, the 700 nm samples fabricated with our equipment show about 5% variation in periodicity which results in about 30% PBG narrowing from the ideal and nearly 10% minimum transmittance [57][14].

Two types of PC structures were fabricated for this work. Samples used for reflectance measurements are regular 3-d structures with a continuous sinusoidal-like profile for the pores. Such samples are shown in **Figure 5** along with an example of current waveform used to generate them. The cross section images reveal that the modulation is slightly skewed to the beginning of the modulation. The vertical period is measured to be 700 nm which is the desired length. Total etched depth is 25 μm and the mean pore diameter is $\bar{d} = 500$ μm. The programmed "modulation index" [15] is about $m_{in} = 0.7$, but results in $m_{etch} \approx 0.1$. Despite this, this structure has good enough optical performance.

---

[13]That is for the current way the PCs are being used: with light coming from the "top" along the pores' axis.

[14]These performance figures were achieved with the latter fabricated samples, with an optimised EE process.

[15]The input waveform is a square signal, so the concept of modulated index in AM is extended here as $m = \max[r(t)]/\min[r(t)]$, where $r(t)$ is the radius of the poresuperfluous.
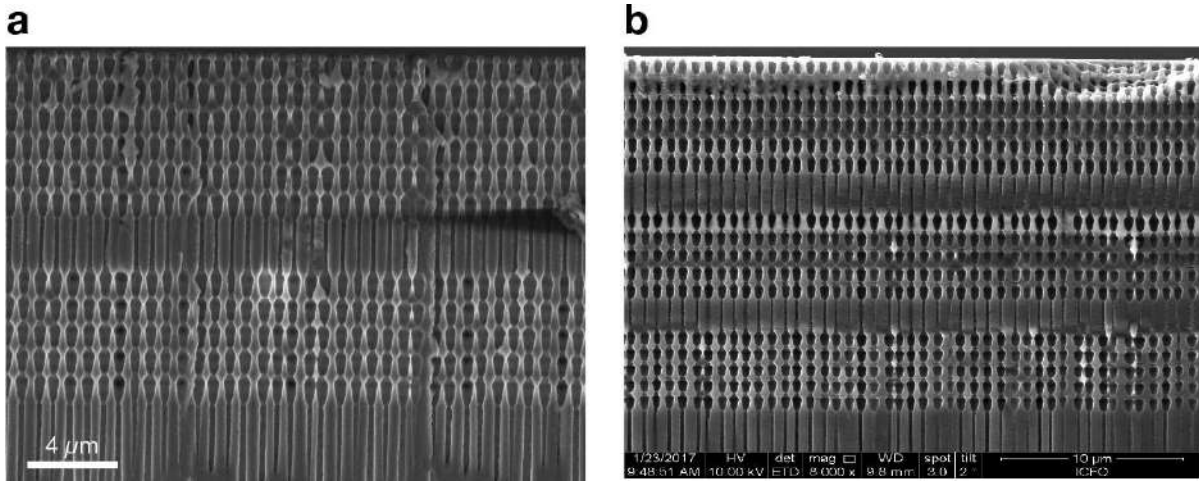
Figure 6. Macroporous silicon structures used in transmission measurements. (a) Is a single defect PC, while (b) shows a two defect MPS structure. Panel (b) © 2017 IEEE. Reprinted, with permission, from [60].

Comparing the etched pore profile from the input waveform (**Figure 5c**), it can be seen that during the high plateau portion of the profile, once the pore has reached its maximum diameter, it slowly starts narrowing as the pore front advances. Presently, this can only be "corrected" by trial and error and judicious changes to the current and potential waveforms. For example, a second profile was designed with smoother transitions and "pre-skewing" resulting however in the PC of **Figure 5b**. Better modulation index was obtained ($m_{etch} \approx 0.2$) but the skewing did not improve. In addition, the vertical period increased to 850 nm, which corresponds to a PBG centred at $\lambda_0 = 5.03\ \mu$m.

Samples used for transmittance measurements include one or more defects, as shown in **Figure 6**. These structures have been fabricated using a refined profile. As seen on the SEM cross-section micrograph, the modulation skew is still present[16], but the vertical period length is better adjusted. Otherwise, the quality of the fabricated structures is maintained. The modulation index has been increased, with pores having a smaller diameter at the necks. This greatly improves the PBG (both width and transmittance blocking) of the PC compared to the first structures depicted in **Figure 5**. The vertical period of the PC used for these samples is $\overline{p}_v \approx 1\ \mu$m. These samples have at least one planar defect in the regular PC profile to define a resonant cavity. These cavities have a diameter $d_{def} = 230$ nm, and length was varied around $l_{def} = 2.1\ \mu$m [60], to place the resonance at $\lambda = 4.25\ \mu$m.

4.1.2. Optical response

Samples were optically characterised after fabrication to ensure the adequacy to sensing CO_2. This was done in a FT-IR spectrometer in reflection mode with light incident at a quasi-normal angle of $\theta_i = 13°$. Also some samples were analysed in transmission mode with light illuminating in normal angle of incidence. The wavelength range of the analysis extends the MIR and some of the NIR regions from $\lambda = 1\ \mu$m to 20 μm.

[16]However for this particular instance, the asymmetric modulation was actually designed.

Samples used for reflectance gas measurements, such as the one in **Figure 5a**, have a single PBG in the optical response. The morphological analysis shows that, as the modulation index is small, the PBG will be relatively narrow. This is confirmed in the measurement shown in **Figure 7**. The results confirm that as expected by the criteria given above, the PBG of a 3-d PC with a vertical period of 700 nm is centred at $\lambda_0 = 4.25$ μm. PC quality and modulation index limit the reflectance to about 30%. In spite of these shortcomings, the obtained response is good enough to be used for the sensing of carbon dioxide.

The samples for transmission measurements have different responses according to the number of PC defects placed. As seen in **Figure 8a**, **b**, placing two defects gives rise to two resonant
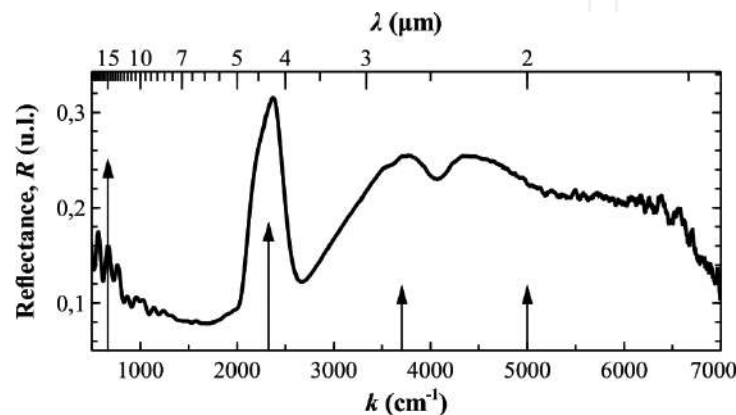
Figure 7. Measured spectra of the PC shown in **Figure 5a**. The absorption lines of CO_2 are marked with arrows, the length giving a qualitative impression of their strength. It can be clearly seen how the PBG of the MPS structure corresponds to the $\lambda = 4.25$ μm absorption line.
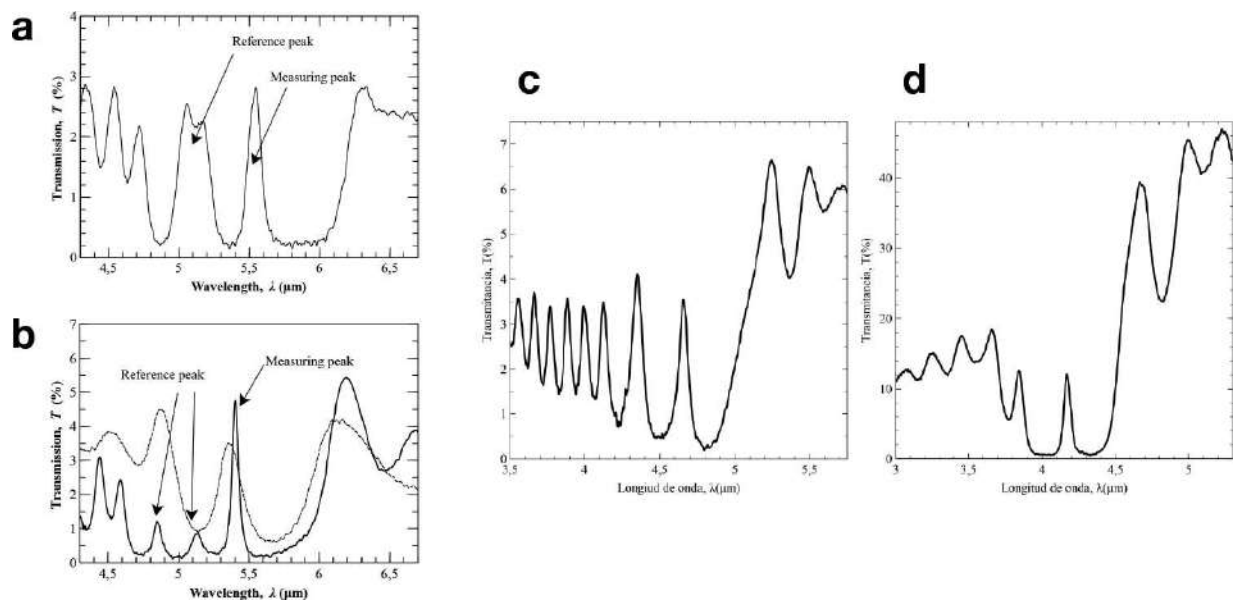
Figure 8. Characterisation of transmission PC samples. (a) Is a two defect sample which shows two resonance states inside the PBG. (b) Is for a three defect PC (thick line) compared to a single defect crystal. (c) Is the characterisation of the sample in **Figure 6b**. (d) Shows the response of a two-defect membrane PC with a peak centred in the CO_2 absorption line at 4.25 μm, and a reference peak at 3.8 μm. Panels (a) and (b) © 2017 IEEE. Reprinted, with permission, from [60]. Panels (c) and (d) from [61] are licensed under CC BY-NC-ND 3.0.

states, and three states if three defects are used. Coupling between resonant cavities induce the appearance of several resonances in the optical spectra even if all cavities are of the same dimensions. The placement of the defect along the PC depth also influences the coupling efficiency and quality factor of the resonance. The creation of a membrane also improves the transmitted signal, compare **Figure 8c** and **d** where the transmitted peak is almost 10% to the 4% of the non-membrane sample.

4.2. Gas measurement system

After the devices were characterised, they were measured under different atmospheres consisting of CO_2 diluted in pure nitrogen. The amount of carbon dioxide was controlled using a two gas mixer in which one line is pure nitrogen as the carrier gas, and the process gas (CO_2 is this case) is connected to the second line. Each line is controllable separately: shutting, pressure, and flow. Both gas lines are then mixed in a manifold and the mixture is then output to the gas cell. The gas cell is sealed with one input port and one exhaust port. The flow control is performed using mass flow controllers (MFCs) of different range: the carrier gas controller (MFC1) is 2 l/min full scale (FS), and the process gas controller (MFC2) is 200 ml/min FS. Both MFCs are calibrated for N_2, so for the process gas a correction factor is used. For the measurements, a constant flow rate of $\dot{V} = 400$ ml/min for the mixture is used. In these conditions, the minimum gas concentration goes from 7500 ppm to 50%. Given the performance data of the MFCs, the concentration uncertainty is given by $B_c^2 \approx c^2 \left[3.15 \cdot 10^{-3} + 0.25 \cdot 10^{-3} \left(c^{-1} - 1 \right)^2 \right]$, where $c = \dot{V}_2 / (\dot{V}_1 + \dot{V}_2)$ is the gas concentration, and $\dot{V}_1$ and $\dot{V}_2$ are the flow rates of carrier and gas, respectively. Note that $\dot{V} = \dot{V}_1 + \dot{V}_2$.

The gas mixture is fed to a gas cell purposely built where the MPS photonic crystal is placed. The gas flows continuously through the cell. For the measurements, a broadband infrared light source is used. This light is directed to the cell and then collected by a photodetector (PD). In the work here presented, the MPS structures were characterised by FT-IR spectrometry. The expected response of an autonomous NDIR measuring device can be then extrapolated from the spectroscopic gathered data in the characterisation of the PCs.

4.2.1. Principle of detection and method

The basic idea here proposed for an NDIR system is to use a MPS photonic crystal with a PBG wide enough to comprise one of the gas absorption *regions*. In the case of CO_2, this region extends from $\lambda \approx 4.20$ to 4.35 μm (see Section 2 – above). Ideally, all light outside the PBG should be discarded and not arrive at the detector. Once the light has been filtered, the photodetector gives a reading proportional to the incoming optical power, and further filtered by the detector's photo-response. In the following discussion, it is assumed that the PD response is flat in the absorption region of the gas.

From the characterisation measurements, it is straightforward to approximate the expected response of the NDIR system. The spectra can be any of the reflectance, transmittance or absorbance, as these are proportional to the power of the electromagnetic wave: $|E_r(\lambda)|^2 = R(\lambda)|E_i(\lambda)|^2$, and so on. Now it is possible to define the quantity $S_R = \int R(\lambda) d\lambda$ as the
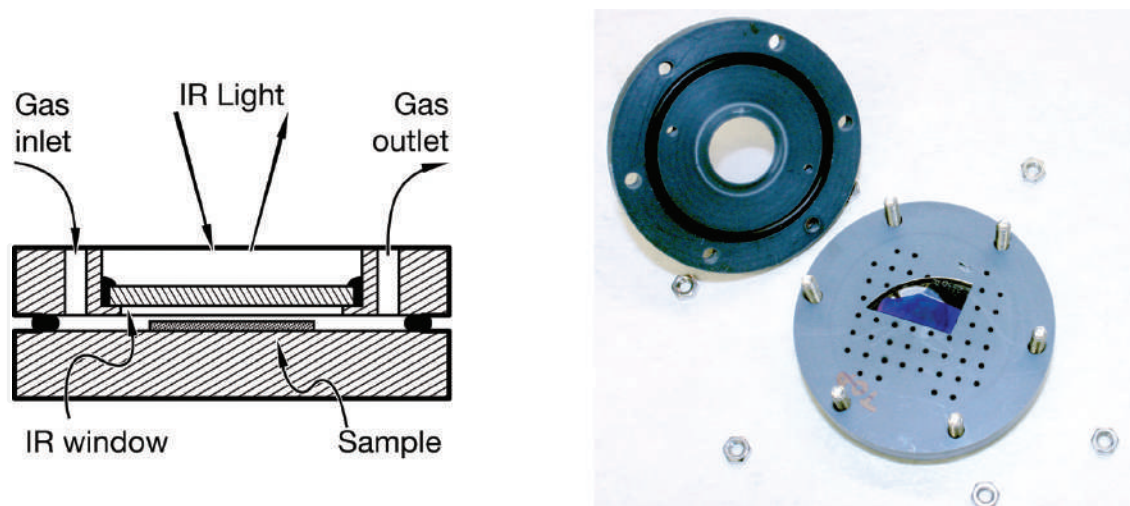
Figure 9. Gas cell for reflection measures. A schematic section view is shown and the actual fabricated cell is pictured next to it. The sample is held in place by locking it with a spring screwed in a suitable position of the cell base grid. The cell is made airtight by an O-ring, and sealant around the IR window.

normalised optical power received at the PD from the reflectance data. S_R is thus proportional to the gas concentration and estimates the actual output of a PD. Equivalent power quantities S_T and S_A can be defined for the transmittance and absorbance spectra respectively. A second measuring criteria is simply evaluating the reflectance spectrum at a given wavelength $R(\lambda_{gas}) = R_{gas}$ (equivalent quantities are defined for transmittance and absorbance). Such wavelength is chosen to be where absorption is the greatest. The relation of this quantity with an actual output of a PD is less clear but serves to evaluate the performance of the gas cell and PC.

4.3. Reflection CO_2 measurement

Reflection measurement of CO_2 uses a PC as a selective reflector. The reflection spectra are obtained from which the absorbance spectra are calculated as $A(\lambda) = 1 - T(\lambda) = 1 - R(\lambda) / R_0(\lambda)$; where $R(\lambda)$ is the measured spectrum at some gas concentration, and $R_0(\lambda)$ is the reference spectrum (only N_2). The "optical power" is then $S = \int A(\lambda)d\lambda$. Using a reference spectrum removes any effect of the optical system, such as reflectance at optical interfaces.

4.3.1. Setup

The measurement setup consists of the gas mixer connected to a specifically built gas cell. A schematic view of the cell design is shown in **Figure 9** alongside the actual built device. The cell consists of two plates separated with an O-ring such that the cell is made airtight. The top plate has one port for gas input and another for output, and a central opening where a potassium bromide (KBr) window is placed and held in place by a sealant. When assembled, the two plates are held by several screw ensuring mechanical stability and airtightness, with the PC underneath the IR window. The gap from the sample to the window is about 0.5 mm, resulting in a total[17] light path of 1 mm.

---

[17]This figure may change due to uncertainty. For example MPS sample thickness or tightening of the screws can change the gap as much as 0.2 mm. It must be remarked that this is a proof-of concept cell.
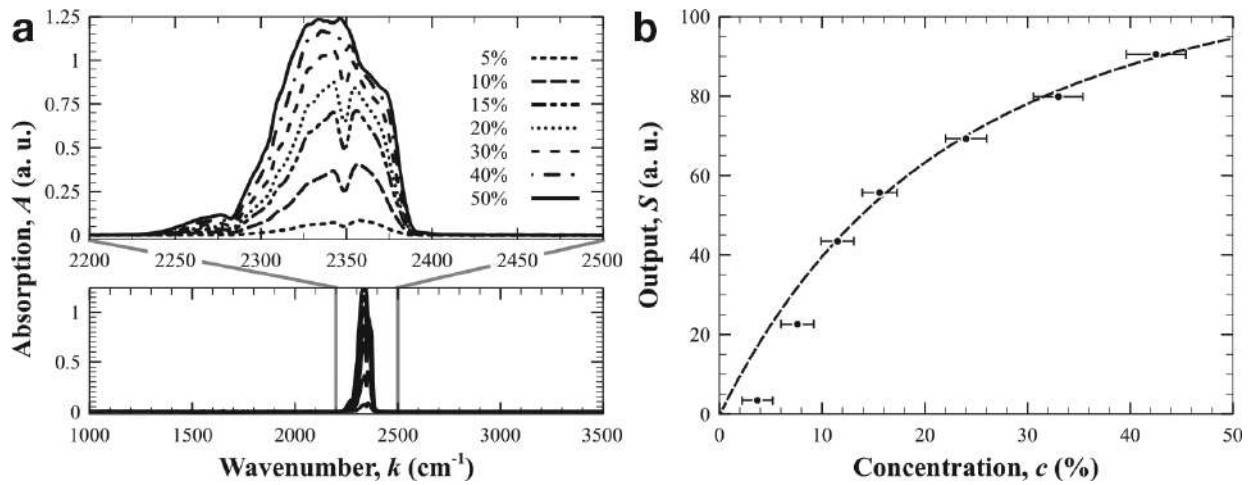
Figure 10. Measurement results for reflectance setup. The spectral response (a) from $k = 1000$ cm^{-1} (10 μm) to 3500 cm^{-1} (2.86 μm) has been normalised to a pure N$_2$ atmosphere and shows the effect of absorption due to CO$_2$ in the $\lambda = 4.25$ μm band. The output response (b) against concentration shows good sensitivity for concentrations above 5%. The dashed line is the ideal Beer–Lambert response.

The cell is then placed in the spectrometer to make the gas concentration readings. In particular, a Renishaw Raman microscope equipped with Smiths IlluminatIR FT-IR module is used to take reflectance measurements at normal incidence, $\theta_i = 0^\circ$. The aperture sizes used in the optical setup was 50 μm $\times$ 50 μm. The wavelength range extends from $k = 1000$ cm^{-1} (10 μm) to 3500 cm^{-1} (2.86 μm). Resolution is 4 cm^{-1}. Each spectrum at a given concentration was averaged over 256 scans.

4.3.2. Results

Reflectance spectra were measured for CO$_2$ at concentrations from 3 to 43%, the results summarised in **Figure 10**. Lower concentrations were tested but for concentrations below 3% changes are very small and difficult to discriminate. This effect is then observed in the "optical power" signal S at the output (**Figure 10b**) calculated as mentioned above. **Figure 10b** also shows that the Beer–Lambert law is closely followed by the measured data for concentrations above 10%. From the fitted B-L model, it is possible to extract the exponential term $l \cdot a \approx 3.65$ (where l is the optical path length, and a the absorption coefficient). From the HiTran data for carbon dioxide, at $\lambda = 4.25$ μm and 4 cm^{-1} instrument resolution, $a_{CO_2} \approx 50$ cm^{-1}. This gives that the effective path length is $l_{eff} \approx 0.75$ mm. Measurement uncertainty is dominated by the mixer uncertainty, as seen in **Figure 10b**, as power measures are averaged over a large number of scans. This results in a fairly constant uncertainty across the full measurement range about $\pm 2\%$.

5. Conclusion

Macroporous silicon is a versatile material that has shown to be a good candidate for the obtainment of PCs for gas sensing applications. Using fabrication methods such as EE opens

up the possibility of obtaining high-quality photonic filters, in large quantities, and economically competitive. Furthermore, this fabrication technique is very flexible allowing creating customised designs with little effort. Using silicon as the base material has other benefits, such as the reutilisation of the existing manufacturing tooling and the reuse of process flows. Moreover, EE is compatible with microfabrication technology and might be incorporated in VLSI designs to build complete sensing devices. This will result in more compact and integrated system design lowering the bill of materials, costs, and improving manufacturability.

Here we demonstrate one possible way to use MPS PCs for gas sensing: as selective filters. Carbon dioxide has been detected and quantified using NDIR reflectance measurements. It has been found the MPS crystal has also an effect in the measured absorption. This is due to the very nature of the PC, slowing the group velocity of the incident light and enhancing the interaction time—increasing the effective optical path length—with the gas mixture. The inclusion of resonant cavities further enhances light absorption by inducing resonant states and spatially confining the IR radiation.

The PCs here shown, prove that a compact CO_2 sensor using MPS technology is feasible, achieving a detection range near to that of commercial optical devices based on IR PD/LED. The devices shown here have room for improvement in particular regarding the fabrication, and progress is steadily being made in this area.

Acknowledgements

Conflict of interest

The authors declare that there is no conflict of interest.

Author details

Didac Vega* and Ángel Rodríguez

*Address all correspondence to: didac.vega@upc.edu

Electronic Engineering Department (EEL), Universitat Politècnica de Catalunya (UPC), Barcelona, Spain

References

[1] Vega Bru D, Rodríguez Martínez Á. Macroporous silicon: Technology and applications. En: Igorevich Talanin V, editor. New Res. Silicon - Struct. Prop. Technol., InTech; 2017. DOI:10.5772/67698

[2] Lehmann V, Föll H. Formation mechanism and properties of electrochemically etched trenches in n-type silicon. Journal of the Electrochemical Society. 1990;**137**:653-659. DOI: 10.1149/1.2086525

[3] Lehmann V. The physics of macropore formation in low doped n-type silicon. Journal of the Electrochemical Society. 1993;**140**:2836. DOI: 10.1149/1.2220919

[4] Lehmann V. The physics of macroporous silicon formation. Thin Solid Films. 1995;**255**:1-4. DOI: 10.1016/0040-6090(94)05620-S

[5] Zhang XG. Mechanism of pore formation on n-type silicon. Journal of the Electrochemical Society. 1991;**138**:3750. DOI: 10.1149/1.2085494

[6] Propst EK. The electrochemical oxidation of silicon and formation of porous silicon in acetonitrile. Journal of the Electrochemical Society. 1994;**141**:1006. DOI: 10.1149/1.2054832

[7] Parkhutik V. Porous silicon—Mechanisms of growth and applications. Solid State Electronics. 1999;**43**:1121-1141. DOI: 10.1016/S0038-1101(99)00036-2

[8] Ho KM, Chan CT, Soukoulis CM. Existence of a photonic gap in periodic dielectric structures. Physical Review Letters. 1990;**65**:3152-3155. DOI: 10.1103/PhysRevLett.65.3152

[9] Pendry JB. Photonic band structures. Journal of Modern Optics. 1994;**41**:209-229. DOI: 10.1080/09500349414550281

[10] Taalbi A, Bassou G, Youcef MM. New design of channel drop filters based on photonic crystal ring resonators. Optik- International Journal of Light and Electron Optics. 2013; **124**:824-827. DOI: 10.1016/j.ijleo.2012.01.045

[11] Lenert A, Rinnerbauer V, Bierman DM, Nam Y, Celanovic I, Soljacic M, et al. 2D Photonic-crystals for high spectral conversion efficiency in solar thermophotovoltaics. Proc. IEEE Int. Conf. Micro Electro Mech. Syst., 2014, p. 576-579. DOI: 10.1109/MEMSYS.2014.6765706

[12] Schilling J, Birner A, Müller F, Wehrspohn RB, Hillebrand R, Gösele U, et al. Optical characterisation of 2D macroporous silicon photonic crystals with bandgaps around 3.5 and 1.3 µm. Optics Materials (Amst). 2001;**17**:7-10. DOI: 10.1016/S0925-3467(01)00012-X

[13] Cheylan S, Trifonov T, Rodriguez A, Marsal LF, Pallares J, Alcubilla R, et al. Visible light emission from macroporous Si. Optics Materials (Amst). 2006;**29**:262-267. DOI: 10.1016/j.optmat.2005.06.021

[14] Vega Bru D, Todorov Trifonov T, Hernández Díaz D, Rodríguez Martínez Á, Alcubilla González R. Blackbody behaviour from spiked macroporous silicon photonic crystals. Spanish Conf. Electron Devices. «8th Spanish Conf. Electron Devices», 2011, p. 257-258

[15] Vega D, Marti F, Rodriguez A, Trifonov T. Macroporous silicon for spectroscopic CO_2 detection. IEEE SENSORS 2014 Proc., Valencia: IEEE; 2014, p. 1061-1064. DOI: 10.1109/ICSENS.2014.6985187

[16] Cardador D, Vega D, Segura D, Trifonov T, Rodr?guez A. Enhanced geometries of macroporous silicon photonic crystals for optical gas sensing applications. Photonics and Nanostructures – Fundamentals and Applications 2017;**25**:46-51. DOI: 10.1016/j.photonics.2017.04.005

[17] Pergande D, Geppert TM, Rhein A von, Schweizer SL, Wehrspohn RB, Moretton S, et al. Miniature infrared gas sensors using photonic crystals. Journal of Applied Physics 2011;**109**:83117. DOI: 10.1063/1.3575176

[18] Geppert TM, Schweizer SL, Schilling J, Jamois C, Rhein AV, Pergande D, et al. Photonic crystal gas sensors. En: Fauchet PM, Braun PV, editores. Opt. Sci. Technol. SPIE 49th Annu. Meet., vol. 5511, Denver, CO: International Society for Optics and Photonics; 2004, p. 61-70. DOI: 10.1117/12.561724

[19] Cai Z, Smith NL, Zhang J-T, Asher SA. Two-dimensional photonic crystal chemical and biomolecular sensors. Analytical Chemistry. 2015;**87**:5013-5025. DOI: 10.1021/ac504679n

[20] Lee H-S, Lee E-H. Design of compact silicon optical modulator using photonic crystal MZI structure. 2008 5th IEEE Int Conf Gr IV Photonics 2008:308-310. DOI: 10.1109/GROUP4.2008.4638182

[21] Viktorovitch P, Drouard E, Garrigues M, Leclercq JL, Letartre X, Rojo Romeo P, et al. Photonic crystals: Basic concepts and devices. Comptes Rendus Physique. 2007;**8**:253-266. DOI: 10.1016/j.crhy.2006.04.005

[22] Threm D, Nazirizadeh Y, Gerken M. Photonic crystal biosensors towards on-chip integration. Journal of Biophotonics. 2012;**5**:601-616. DOI: 10.1002/jbio.201200039

[23] YOLE. YOLE Reports abstract for EPIC. 2015

[24] MNT Gas Sensor Forum. MNT Gas Sensor Roadmap. 2006

[25] Sekhar PK, Brosha EL, Mukundan R, Garzon FH. Chemical sensors for environmental monitoring and homeland security. Electrochemical Society Interface. 2010:35-40. DOI: 10.1149/2.F04104if

[26] Ramboll Environ US Corporation. Technology Assessment Report: Air Monitoring Technology near Upstream Oil and Gas Operations. 2017

[27] Wetchakun K, Samerjai T, Tamaekong N, Liewhiran C, Siriwong C, Kruefu V, et al. Semiconducting metal oxides as sensors for environmentally hazardous gases. Sensors and Actuators B: Chemical. 2011;**160**:580-591. DOI: 10.1016/j.snb.2011.08.032

[28] OECD. Smart Sensor Networks : Technologies and Applications for Green Growth. 2009

[29] Tonouchi M. Cutting-edge terahertz technology. Nature Photonics. 2007;**1**:97-105. DOI: 10.1038/nphoton.2007.3

[30] Bigourd D, Cuisset A, Hindle F, Matton S, Fertein E, Bocquet R, et al. Detection and quantification of multiple molecular species in mainstream cigarette smoke by continuous-wave terahertz spectroscopy. Optics Letters. 2006;**31**:2356. DOI: 10.1364/OL.31.002356

[31] Lee DD. Environmental gas sensors. IEEE Sensors Journal. 2001;**1**:214-224. DOI: 10.1109/JSEN.2001.954834

[32] Han X, Naeher LP. A review of traffic-related air pollution exposure assessment studies in the developing world. Environment International. 2006;**32**:106-120. DOI: 10.1016/j.envint.2005.05.020

[33] Monn C. Exposure assessment of air pollutants: A review on spatial heterogeneity and indoor/outdoor/personal exposure to suspended particulate matter, nitrogen dioxide and ozone. Atmospheric Environment. 2001;**35**:1-32. DOI: 10.1016/S1352-2310(00)00330-7

[34] U.S. Environmental Protection Agency. American's Children and the Environment. 3rd ed. 2013

[35] Rothman LS, Gordon IE, Barbe A, Benner DC, Bernath PF, Birk M, et al. The HITRAN 2008 molecular spectroscopic database. Journal of Quantitative Spectroscopy and Radiation Transfer. 2009;**110**:533-572. DOI: 10.1016/j.jqsrt.2009.02.013

[36] Dinh T-V, Choi I-Y, Son Y-S, Kim J-C. A review on non-dispersive infrared gas sensors: Improvement of sensor detection limit and interference correction. Sensors and Actuators B: Chemical. 2016;**231**:529-538. DOI: 10.1016/j.snb.2016.03.040

[37] Mikuta R, Silinskas M, Bourouis R, Kloos S, Burte EP. Characterization of non-dispersive infrared gas detection system for multi gas applications. tm - Tech Mess. 2016;**83**:410-416. DOI: 10.1515/teme-2015-0010

[38] Painter O, Vučković J, Scherer A. Defect modes of a two-dimensional photonic crystal in an optically thin dielectric slab. Journal of Optical Society of America B. 1999;**16**:275. DOI: 10.1364/JOSAB.16.000275

[39] Nagahara K, Morifuji M, Kondow M. Optical coupling between a cavity mode and a waveguide in a two-dimensional photonic crystal. Photonics Nanostructures - Fundamental Applications. 2011;**9**:261-268. DOI: 10.1016/j.photonics.2011.04.011

[40] Hu J. Ultra-sensitive chemical vapor detection using micro-cavity photothermal spectroscopy. Optics Express. 2010;**18**:22174. DOI: 10.1364/OE.18.022174

[41] Vasiliev A, Malik A, Muneeb M, Kuyken B, Baets R, Roelkens G. On-chip mid-infrared Photothermal spectroscopy using suspended silicon-on-insulator microring resonators. ACS Sensors. 2016;**1**:1301-1307. DOI: 10.1021/acssensors.6b00428

[42] Wehrspohn RB, Schweizer SL, Gesemann B, Pergande D, Geppert TM, Moretton S, et al. Macroporous silicon and its application in sensing. Comptes Rendus Chimie. 2013;**16**:51-58. DOI: 10.1016/j.crci.2012.05.011

[43] Xu H, Wu P, Zhu C, Elbaz A, Gu ZZ. Photonic crystal for gas sensing. Journal of Materials Chemistry C. 2013;**1**:6087. DOI: 10.1039/c3tc30722k

[44] Śmigaj W, Gralak B. Validity of the effective-medium approximation of photonic crystals. Physical Review B. 2008;**77**:235445. DOI: 10.1103/PhysRevB.77.235445

[45] Li HH. Refractive index of silicon and germanium and its wavelength and temperature derivatives. Journal of Physical and Chemical Reference Data. 1980;**9**:561. DOI: 10.1063/1.555624

[46] Garín M, Trifonov T, Hernández D, Rodriguez A, Alcubilla R. Thermal emission of macroporous silicon chirped photonic crystals. Optics Letters. 2010;**35**:3348-3350. DOI: 10.1364/OL.35.003348

[47] Declair S, Meier T, Zrenner A, Förstner J. Numerical analysis of coupled photonic crystal cavities. Photonics Nanostructures - Fundamental Applications. 2011;**9**:345-350. DOI: 10.1016/j.photonics.2011.04.012

[48] Kolasinski KW. Etching of silicon in fluoride solutions. Surface Science. 2009;**603**:1904-1911. DOI: 10.1016/j.susc.2008.08.031

[49] Trifonov T, Rodríguez A, Marsal LF, Pallarès J, Alcubilla R. Macroporous silicon: A versatile material for 3D structure fabrication. Sensors and Actuators A: Physical. 2008; **141**:662-669. DOI: 10.1016/j.sna.2007.09.001

[50] Rönnebeck S, Ottow S, Carstensen J, Föll H. Crystal orientation dependence of macropore formation in n-Si with backside-illumination in HF-electrolyte. Journal of Porous Materials. 2000;**7**:353-356. DOI: 10.1023/A:1009639105357

[51] Carstensen J, Prange R, Föll H. A model for current-voltage oscillations at the silicon electrode and comparison with experimental results. Journal of the Electrochemical Society. 1999;**146**:1134-1140. DOI: 10.1149/1.1391734

[52] Föll H, Christophersen M, Carstensen J, Hasse G. Formation and application of porous silicon. Material Science and Engineering R Reports. 2002;**39**:93-141. DOI: 10.1016/S0927-796X(02)00090-6

[53] Carstensen J, Christophersen M, Hasse G, Föll H. Parameter dependence of pore formation in silicon within a model of local current bursts. Physica Status Solidi. 2000;**182**:63-69. DOI: 10.1002/1521-396X(200011)182:1<63::AID-PSSA63>3.0.CO;2-E

[54] Hilbrich S, Theiβ W, Arens-Fischer R, Glück O, Berger M. The influence of the doping level on the optical properties of porous silicon. Thin Solid Films. 1996;**276**:231-234. DOI: 10.1016/0040-6090(95)08060-0

[55] Vega Bru D, Cardador Maza D, Trifonov T, Garin Escriva M, Rodriguez MA. The effect of absorption losses on the optical behaviour of macroporous silicon photonic crystal selective filters. Journal of Light Technology. 2016;**34**:1281-1287. DOI: 10.1109/JLT.2015.2503354

[56] Matthias S, Hillebrand R, Müller F, Gösele U. Macroporous silicon: Homogeneity investigations and fabrication tolerances of a simple cubic three-dimensional photonic crystal. Journal of Applied Physics. 2006;**99**:113102. DOI: 10.1063/1.2200871

[57] Segura D, Vega D, Cardador D, Rodriguez A. Effect of fabrication tolerances in macroporous silicon photonic crystals. Sensors Actuators, A Physics. 2017;**264**:172-179. DOI: 10.1016/j.sna.2017.07.011

[58] Langtry TN, Asatryan AA, Botten LC, de Sterke CM, McPhedran RC, Robinson PA. Effects of disorder in two-dimensional photonic crystal waveguides. Physical Review E 2003;**68**:26611. DOI: 10.1103/PhysRevE.68.026611

[59] Schilling J, Scherer A. 3D photonic crystals based on macroporous silicon: Towards a large complete photonic bandgap. Photonics Nanostructures - Fundamental Applications. 2005;**3**:90-95. DOI: 10.1016/j.photonics.2005.09.015

[60] Cardador D, Segura D, Vega D, Rodriguez A. Coupling defects in macroporous silicon photonic crystals. 2017 Spanish Conf. Electron Devices, Barcelona, Spain: IEEE; 2017, p. 1-3. DOI: 10.1109/CDE.2017.7905236

[61] Granados MJ. Fabricación de dispositivos fotónicos integrados. Bachelor's degree Thesis. Universistat Politècnica de Catalunya; 2017

[62] Joannopoulos JD, Johnson SG, Winn JN, Meade RD. Photonic Crystals: Molding the Flow of Light. 2.ª ed. Princeton University Press; 2011

We are IntechOpen,
the world's leading publisher of
Open Access books
Built by scientists, for scientists

6,300
Open access books available

171,000
International authors and editors

190M
Downloads

Our authors are among the

154
Countries delivered to

TOP 1%
most cited scientists

12.2%
Contributors from top 500 universities

Interested in publishing with us?
Contact book.department@intechopen.com

Numbers displayed above are based on latest data collected.
For more information visit www.intechopen.com

New Approach to Mach-Zehnder Interferometer (MZI) Cell Based on Silicon Waveguides for Nanophotonic Circuits

Trung-Thanh Le

Abstract

In this chapter, we present a new scheme for Mach-Zehnder Interferometer (MZI) structure based on only one 4×4 multimode interference (MMI) coupler. We design the new MZI cell on the silicon on insulator (SOI) platform. The MZI based on directional coupler and 2×2 MMI coupler is also investigated in detail. The new MZI cell is a basic building block for photonic applications such as optical quantum gate, optical computing and reconfigurable processors. The numerical simulations show that our approach has advantages of compact size, ease of fabrication with the current complementary metal oxide semiconductor (CMOS) circuitry.

Keywords: multimode interference, silicon on insulator, multimode waveguide, directional coupler, finite difference time difference, finite difference method, modified effective index method

1. Introduction

Mach-Zehnder Interferometer (MZI) structure is a versatile component for photonic integrated circuits. A variety of photonic functional devices can be realized by using the MZI such as optical filter [1], add-drop multiplexer [2, 3], switch [4], modulator [5], sensor [6–8], tunable coupler [9, 10], signal transforms [11–13] and optical computing [14, 15], and so on.

In recent years, we have presented some approaches to realize optical signal processing based on MZI incorporated with microring resonators and multimode interference (MMI) coupler on a silicon on insulator (SOI) platform [16–20]. Silicon photonics is considered a key technology

for next generation optical interconnects, optical computing, data center and communication systems due to its low power operation, compactness, scalability and compatibility with the CMOS process. The SOI platform has a large index contrast between the silicon core and the silicon oxide/air cladding, thus allowing for small bend waveguides and denser integration of photonic components. Silicon photonic devices are also being considered for wavelength-division multiplexing (WDM) metro and long haul network segments.

It was shown that MZI is a basic element (basic cell) for optical photonic circuits and quantum technologies [21]. In [21], by cascading 15 MZIs with 30 thermo-optic phase shifters, a single programmable optical chip has been implemented. In [22], the author has presented a self-aligned universal beam coupler based on MZI elements that can take an arbitrary monochromatic input beam and, automatically and without any calculations, couple it into a single-mode guide or beam. This device can be used for special optical applications such as automatic compensation for misalignment and defocusing of an input beam, coupling of complex modes or multiple beams from fibers or free space to single-mode guides, and retaining coupling to a moving source. By using recursive algorithm, any discrete finite dimensional unitary operator based on MZI elements can also be constructed [23]. In addition, it was shown that optical neural networks based on architecture of 56 MZIs with 213 thermo-optic phase shifter elements have been implemented successfully [24]. This photonic circuit has been fabricated in an SOI platform with OpSIS (University of Washington's Optoelectronic Systems Integration in Silicon) foundry. An optical neuromorphic computing on a vowel recognition dataset has been demonstrated experimentally.

Very recently, universal multiport photonic interferometers by means of arrangements of reconfigurable MZIs on SOI platform can implement any arbitrary unitary transformation between input and output optical modes [25]. These arbitrary transforms are essential to support advanced optical functions such as linear quantum optical gates and circuits, microwave photonics signal processors, spatial mode converters, data center connections and optical networking functionalities. The triangle, square arrangements of MZI elements for hardware architecture are similar to the design principles of the field programmable gate arrays (FPGAs) in electronics. The core concept is to use a large network of identical two-dimensional unit or lattice cells implemented by means of MZIs. With a proper MZI element lattice arrangement, the architecture can implement a variety of functional configurations by mapping the desired matrix to a selection of signal paths through the architecture. By introducing the phase shifter elements in two arms of the MZI, a reconfigurable architecture can be implemented.

In the literature, the MZI consists of two 3 dB 2×2 directional couplers or 2×2 MMI couplers linked though two waveguide arms. It was shown that directional coupler is very sensitive to the fabrication error [16]. The power coupling ratios can be controlled by adjusting the coupling length and/or the gap between the two waveguides of the directional coupler [16]. In practice, accurate fabrication of the gap requires very tight control of the fabrication process. Moreover, additional loss due to mode conversion loss has been found to be a problem [26]. In contrast, MMI-based devices often have large fabrication tolerance, wide operation bandwidth and compact size. As a result, it is attractive to realize new functional devices based on MMIs for photonic applications.

In this chapter, we present a new MZI element architecture based on only one 4×4 MMI coupler on an SOI platform. The phase shifter based on a PN junction, which use the plasma

dispersion effect in silicon waveguides, is used. Our approach has advantages of compact size, ease of fabrication with the current CMOS circuit.

2. MZI cell based on directional couplers

2.1. Directional coupler type I

Figure 1 shows a general configuration of an MZI element based on two-directional couplers type I. Two arms of the MZI use two phase shifters with phase shifts ϕ_1 and ϕ_2. In our study, we use the PN junction operated in reverse bias, the depletion region is widened which lowers the overlap of the optical mode with charge carriers [5, 27]. As a result, the optical loss is low
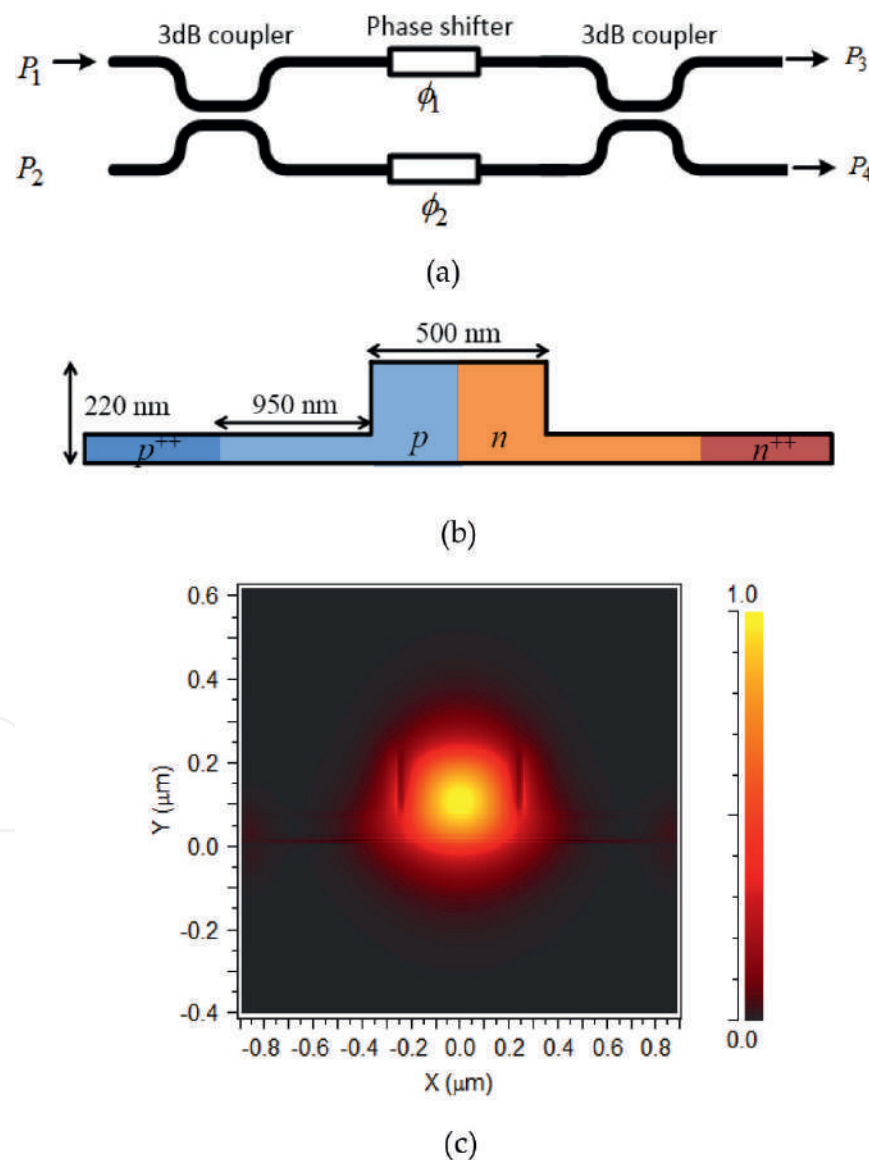
Figure 1. MZI cell based on directional coupler type I.

and the real part of the phase can be significantly increased compared with the forward bias. The change in index of refraction is phenomenologically described by Soref and Bennett model [28]. Here we focus on the central operating wavelength of around 1550 nm.
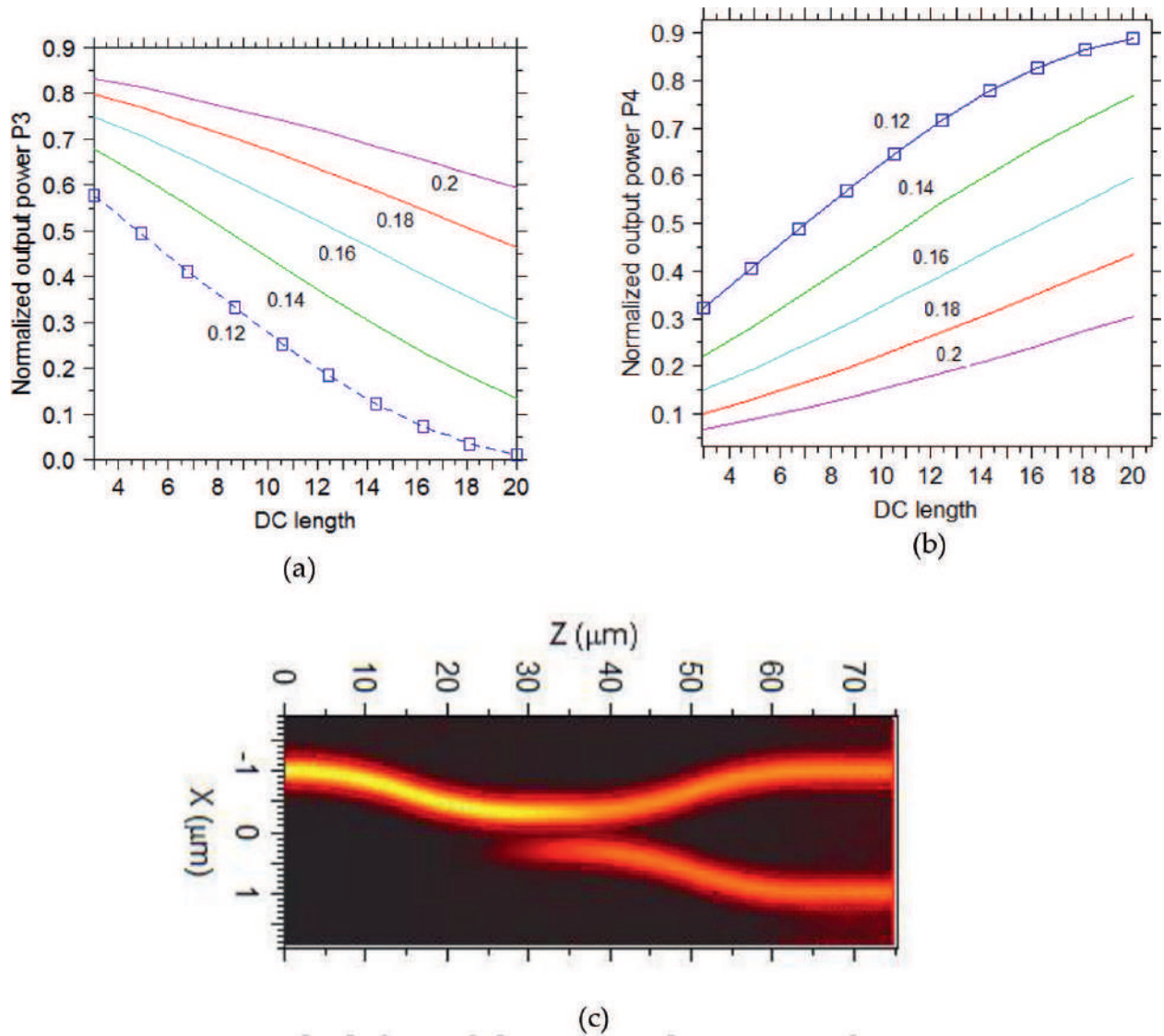
The change in refractive index Δn is described by:

$$\Delta n \,(\text{at } 1550 \ \text{nm}) \quad = \quad -8.8 \times 10^{-22} \Delta N - 8.5 \times 10^{-18} \Delta P^{0.8} \tag{1}$$

The change in absorption $\Delta \alpha$ is described by:

$$\Delta \alpha \,(\text{at } 1550 \ \text{nm}) \quad = \quad 8.5 \ \times 10^{-18} \Delta N + 6 \times 10^{-18} \Delta P \ \left[\text{cm}^{-1} \right] \tag{2}$$

where ΔN and ΔP are the free carriers concentrations of electrons and holes, respectively.

Figure 2. (a), (b) directional coupler design, type I for different separation between two waveguides g = 120, 140, 160, 180 and 200 nm and (c) field propagation at optimal length.

The directional coupler can be characterized by a matrix [29]:

$$M_{DC} = \begin{pmatrix} t & jr \\ jr & t \end{pmatrix} \tag{3}$$

where t and r are the transmission and coupling coefficients of the coupler. The transfer matrix method is used to analyze the working principle of an MZI element. The relationship matrix between the input and output fields of the MZI can be expressed as [30].

$$S = \begin{bmatrix} t & jr \\ jr & t \end{bmatrix} \begin{bmatrix} e^{j\phi_1} & 0 \\ 0 & e^{j\phi_2} \end{bmatrix} \begin{bmatrix} t & jr \\ jr & t \end{bmatrix} = \begin{pmatrix} t^2 e^{j\phi_1} - r^2 e^{j\phi_2} & jrt(e^{j\phi_1} + e^{j\phi_2}) \\ jrt(e^{j\phi_1} + e^{j\phi_2}) & t^2 e^{j\phi_2} - r^2 e^{j\phi_1} \end{pmatrix} \tag{4}$$

where t and r are optical field transmission and cross-coupling coefficients, respectively. For a 3 dB coupler, $r = t = 0.707$ [6, 13], the transfer matrix of the MZI is expressed by:

$$S = je^{j\frac{\Delta\phi}{2}} \begin{bmatrix} \sin\dfrac{\Delta\phi}{2} & \cos\dfrac{\Delta\phi}{2} \\ \cos\dfrac{\Delta\phi}{2} & -\sin\dfrac{\Delta\phi}{2} \end{bmatrix} \tag{5}$$

where $\Delta\phi = \phi_1 - \phi_2$ is the phase shift difference between two arms.

A type I directional coupler is shown in **Figure 1**. This coupler consists of two adjacent waveguides with sine shapes separated by a coupler gap g. The normalized output powers or t^2, r^2 at different directional coupler (DC) length for coupler gap g = 120, 140, 160, 180 and 200 nm are shown in **Figure 2**. From these simulation results, we can achieve the optimal length of the directional coupler for 50:50 coupling ratio or 3 dB coupler. **Figure 2(c)** shows a field propagation for a 3 dB coupler with g = 120 nm and optimal length of 5 μm.
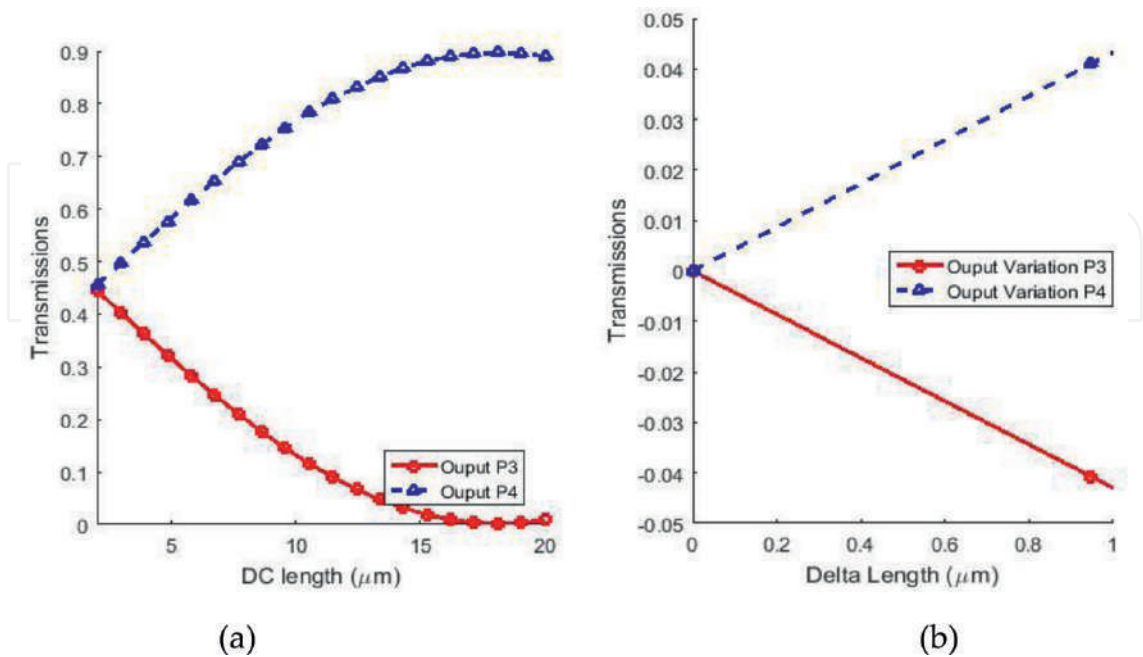
2.2. Directional coupler type II

An MZI cell based on a type II directional coupler is shown in **Figure 3**. The coupler consists of two adjacent waveguides with sine shape and rectangular shape separated by a coupler gap g. The normalized output powers or t^2, r^2 at different directional coupler (DC) length for coupler gap g = 120, 140, 160, 180 and 200 nm are shown in **Figure 4**. From these simulation results, we can achieve the optimal length of the directional coupler for 50:50 coupling ratio or 3 dB coupler. **Figure 4(c)** shows a field propagation for a 3 dB coupler with g = 120 nm and optimal length of 2μm.


Figure 3. MZI cell based on directional coupler type II.

(a) Output power P3

(b) Output power P4

(c) Field propagation gap=120nm at optimal DC length of 2μm
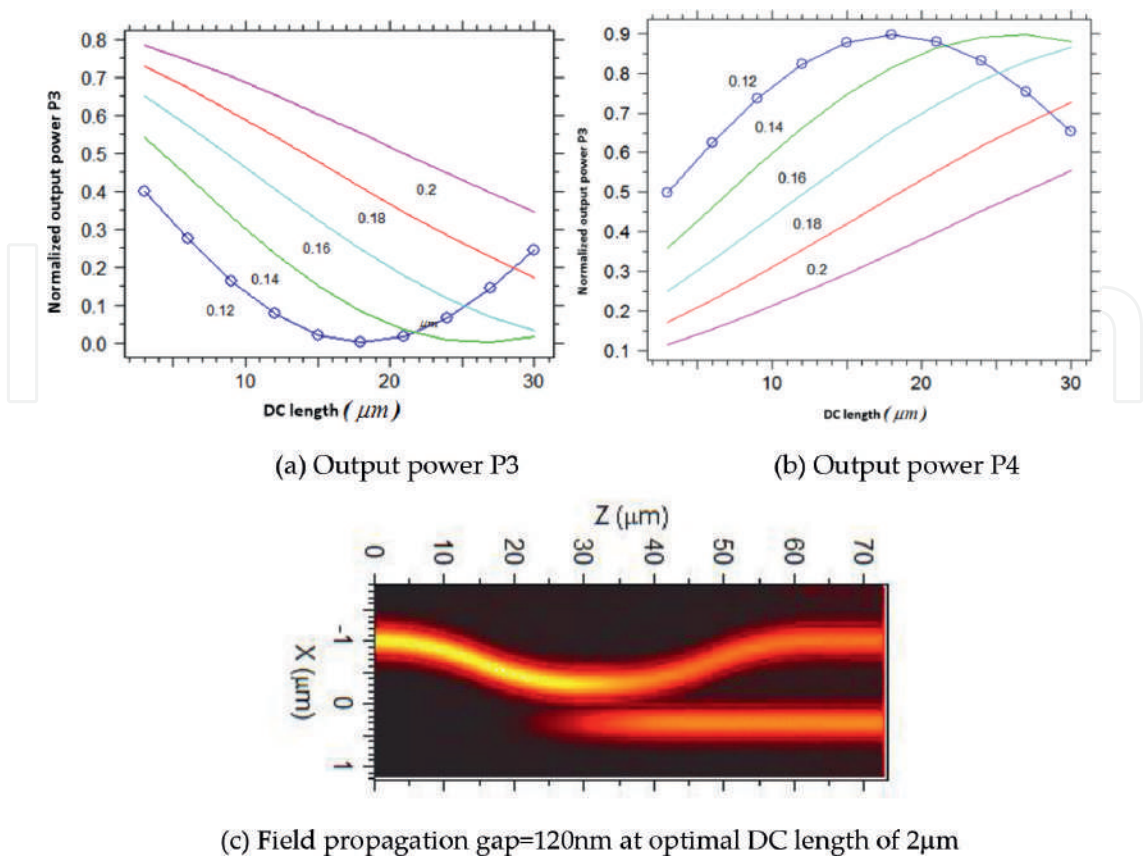
Figure 4. (a), (b) directional coupler design, type II for different separation between two waveguides g = 120, 140, 160, 180 and 200 nm and (c) field propagation at optimal length.

(a)

(b)

Figure 5. Transmissions of the directional coupler type II at different DC length.
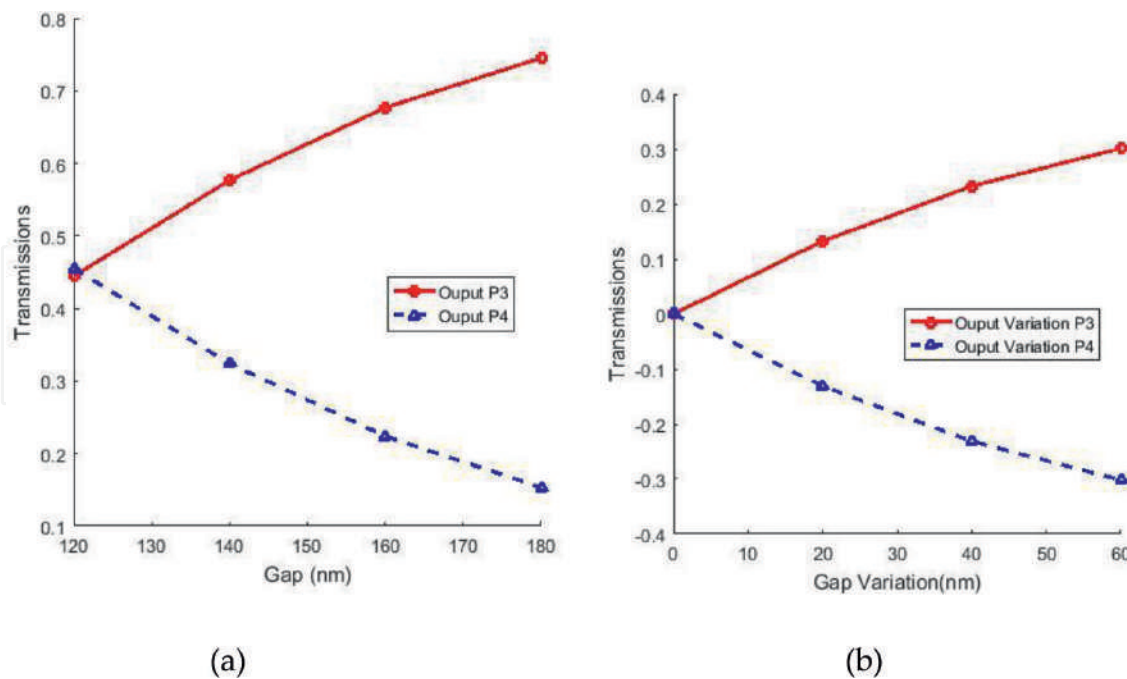
Figure 6. Transmissions of the directional coupler type II at different gap separation.

2.3. Fabrication tolerance analysis

Without loss of generality, we consider the directional coupler type II at the gap separation g = 120 nm for fabrication tolerance analysis. The fabrication tolerance of the directional coupler type I is similar to type II. The normalized output powers at the outputs are shown in **Figure 5**. We can see that a variation in length of ±100 nm results in a variation of 0.01 in normalized output powers. A change in a gap separation of ±10 nm will result in a change of 0.2 in normalized output power. As a result, the directional coupler type II is particularly sensitive to the fabrication error (**Figure 6**).

3. MZI cell based on 2 × 2 multimode interference coupler

The operation of an MMI coupler is based on the self-imaging principle or Talbot effect [31, 32]. The self-imaging shows that an input field is reproduced in single or multiple images at periodic intervals along the propagation direction of the MMI waveguide. The multimode waveguide is large enough to support a large number of modes.

There are two ways to create a 3 dB coupler based on MMI principle [20]: the first is the general interference (GI) mechanism which is independent of the modal excitation (we call MMI coupler type I in this chapter). The second is the restricted interference (RI) mechanism (MMI type II), in which excitation inputs are placed at some special positions so that certain modes are not excited.

3.1. MMI coupler type I

The MZI cell based on MMI couplers type I (GI-MMI) is shown in **Figure 7**. The MZI consists of two 3 dB MMI coupler. We have shown for the first time that a 3 dB GI-MMI coupler at the length of $1.5L_\pi$, where L_π is the beat length of the MMI coupler, can be expressed by a matrix [16]:

$$\mathbf{M}_{MMI,\,TypeI} = \frac{e^{j\phi_{GI}}}{\sqrt{2}} \begin{pmatrix} 1 & -j \\ -j & 1 \end{pmatrix}$$

(6)

where ϕ_{GI} is a constant phase of the coupler.

$$\mathbf{S} = \frac{e^{j\phi_{GI}}}{\sqrt{2}} \begin{pmatrix} 1 & -j \\ -j & 1 \end{pmatrix} \begin{pmatrix} e^{j\phi_1} & 0 \\ 0 & e^{j\phi_2} \end{pmatrix} \frac{e^{j\phi_{GI}}}{\sqrt{2}} \begin{pmatrix} 1 & -j \\ -j & 1 \end{pmatrix} = je^{j2\phi_{GI}}e^{j\frac{\Delta\varphi}{2}} \begin{pmatrix} \sin\dfrac{\Delta\varphi}{2} & \cos\dfrac{\Delta\varphi}{2} \\ \cos\dfrac{\Delta\varphi}{2} & -\sin\dfrac{\Delta\varphi}{2} \end{pmatrix}$$

(7)

The first step is to optimize the MMI sections: we use tapered waveguides with a length of 3 μm for access waveguides in order to improve the device performance. The multimode sections need to be wide enough to achieve good performance and to be spaced apart sufficiently to limit crosstalk between the adjacent access waveguides. By using the numerical simulations, we choose the width of the MMI waveguide is 3 μm. The three-dimensional beam propagation method (3D-BPM) is used to carry out the simulations for the device having a length of 52.2 μm. The aim of this step is to find roughly the positions which result in a power splitting of 50/50, that is, a 3 dB coupler. Then, the 3D-BPM is used to perform the simulations around these positions to locate the best lengths. The normalized output powers of the 2×2 GI-MMI coupler at different lengths of the couplers are plotted in **Figure 8**. The field propagations at the optimal length through the 3 dB GI-MMI coupler and the MZI cell are shown in

(a) MZI based on 3dB GI-MMI

(b) 3dB GI-MMI

(c) Field propagation through an MZI
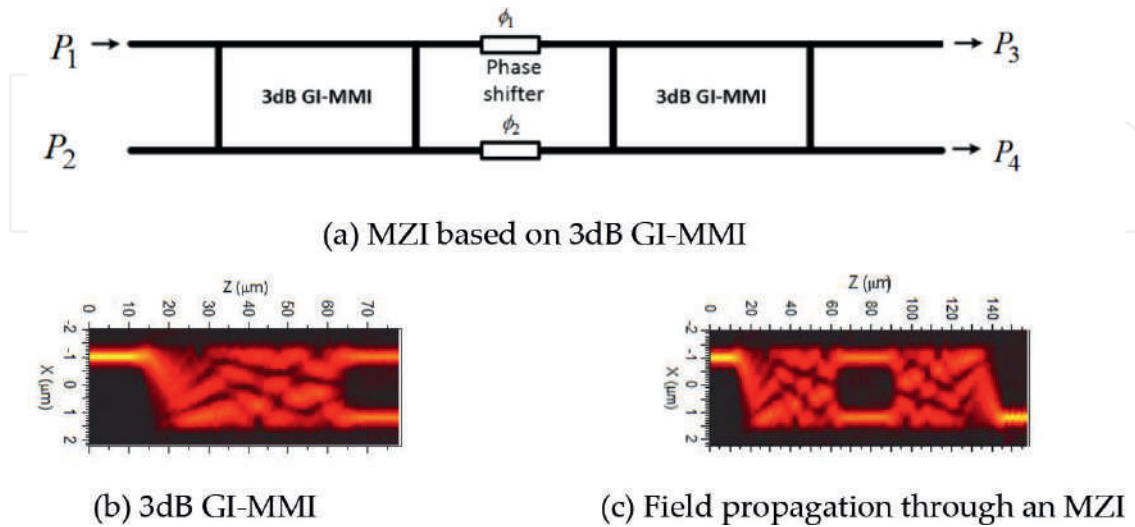
Figure 7. MZI cell based on 3 dB MMI type I.
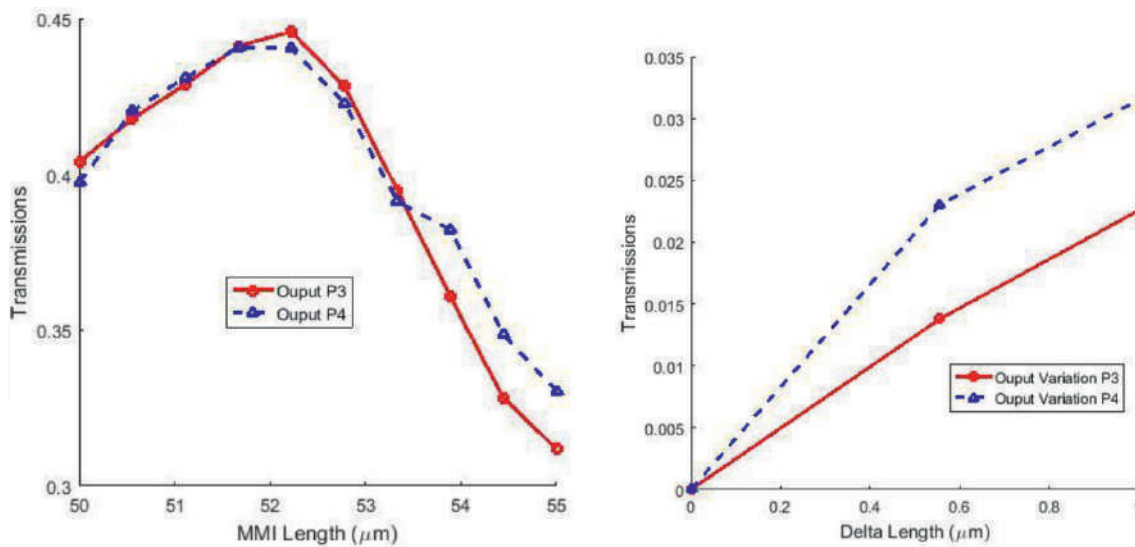
Figure 8. MZI cell based on 3 dB MMI type I.

Figure 7(b) and **(c)**. The simulations show that a variation in MMI length of ±100 nm will result in a change of 0.005 in normalized powers as shown in **Figure 8(b)**. Therefore, the MMI coupler has a much large fabrication tolerance compared with the directional coupler.

3.2. MMI coupler type II

The MZI cell based on MMI couplers type II (RI-MMI) is shown in **Figure 9**. We have shown that a 3 dB RI-MMI coupler at the length of $0.5L_\pi$, where L_π is the beat length of the MMI coupler, can be expressed by a matrix [16]:

$$\mathbf{M}_{MMI,\,TypeII} = \frac{e^{j\phi_{RI}}}{\sqrt{2}} \begin{pmatrix} 1 & j \\ j & 1 \end{pmatrix} \tag{8}$$

where ϕ_{RI} is a constant phase of the coupler.

$$\mathbf{S} = \frac{e^{j\phi_{RI}}}{\sqrt{2}} \begin{pmatrix} 1 & j \\ j & 1 \end{pmatrix} \begin{pmatrix} e^{j\phi_1} & 0 \\ 0 & e^{j\phi_2} \end{pmatrix} \frac{e^{j\phi_{RI}}}{\sqrt{2}} \begin{pmatrix} 1 & j \\ j & 1 \end{pmatrix} = je^{j2\phi_{RI}}e^{j\frac{\Delta\varphi}{2}} \begin{pmatrix} \sin\frac{\Delta\varphi}{2} & \cos\frac{\Delta\varphi}{2} \\ \cos\frac{\Delta\varphi}{2} & -\sin\frac{\Delta\varphi}{2} \end{pmatrix} \tag{9}$$

By using the numerical simulations, we choose the width of the MMI waveguide is 4 μm. The 3D-BPM is used to carry out the simulations for the device having a length of 33.4 μm. The normalized output powers of the 2 × 2 RI-MMI coupler at different lengths of the couplers are plotted in **Figure 10(a)**. The field propagations at the optimal length through the 3 dB RI-MMI coupler and the MZI cell are shown in **Figure 9(b)** and **(c)**. The simulations show that a variation in MMI length of ±100 nm will result in a change of 0.005 in normalized powers as shown in **Figure 10(b)**.
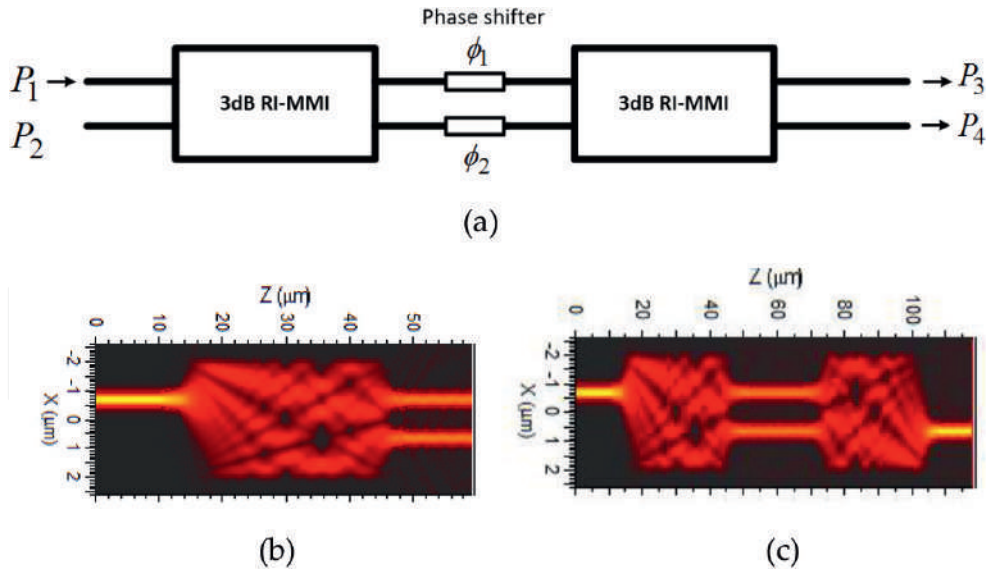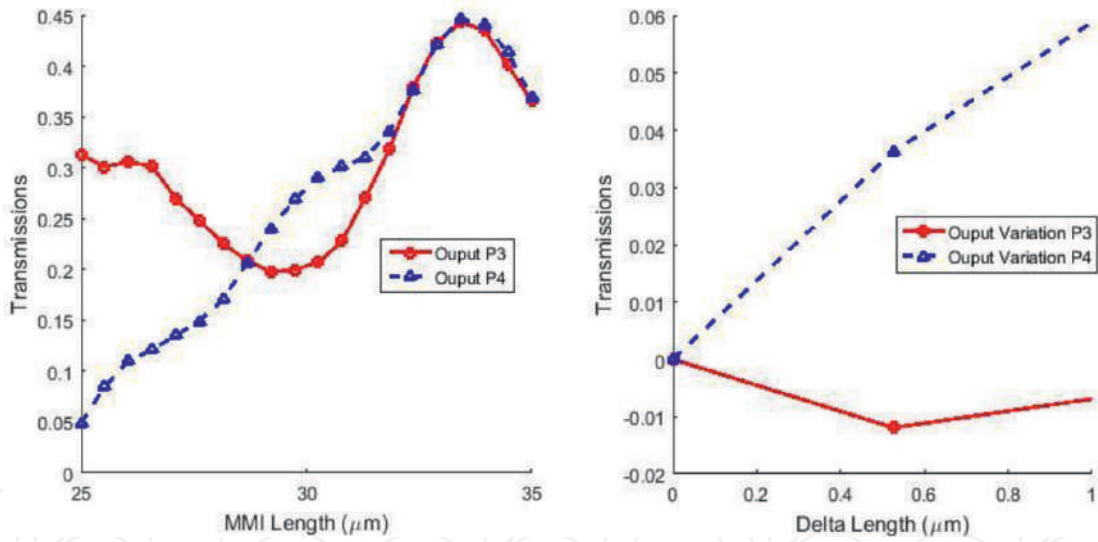
Figure 9. MZI cell based on 3 dB MMI type II.

Figure 10. MZI cell based on 3 dB MMI type II.

4. MZI cell based on a 4 × 4 MMI coupler

Figure 11 shows the new scheme of our new proposed MZI cell based on only one 4 × 4 MMI coupler. We choose the width of the 4 × 4 MMI coupler is 6 μm. The optimal length of the MMI is calculated by the 3D-BPM [33]. We show that the optimal length is found to be 115.8 μm. Figure 11(b) and (c) shows the field propagation through the 4 × 4 MMI coupler at the optimal length for input signal at port 1 and port 2, respectively.

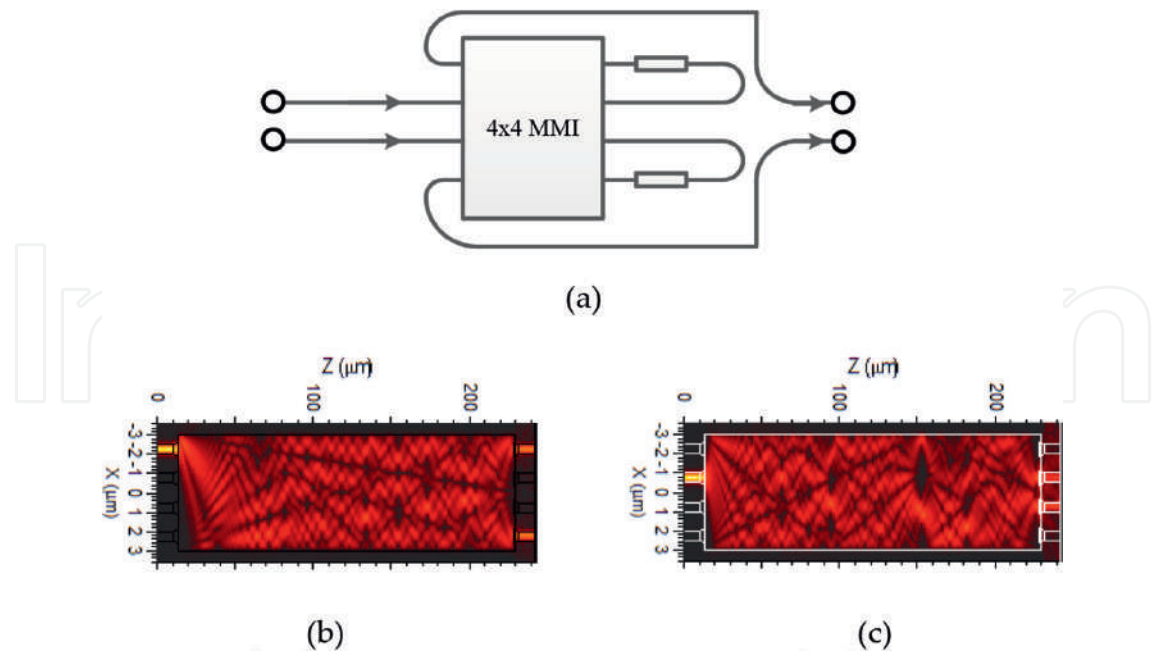Figure 12 shows the normalized output powers at output port 1 and 4 while the input signal is at input port 1.

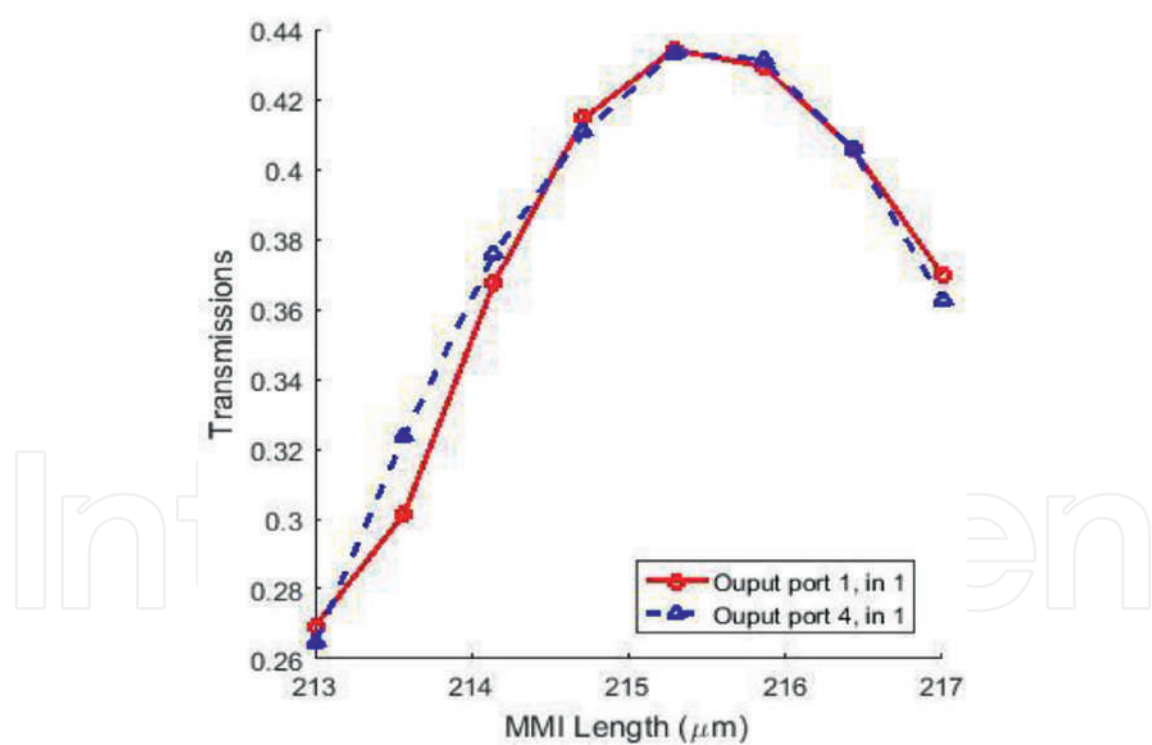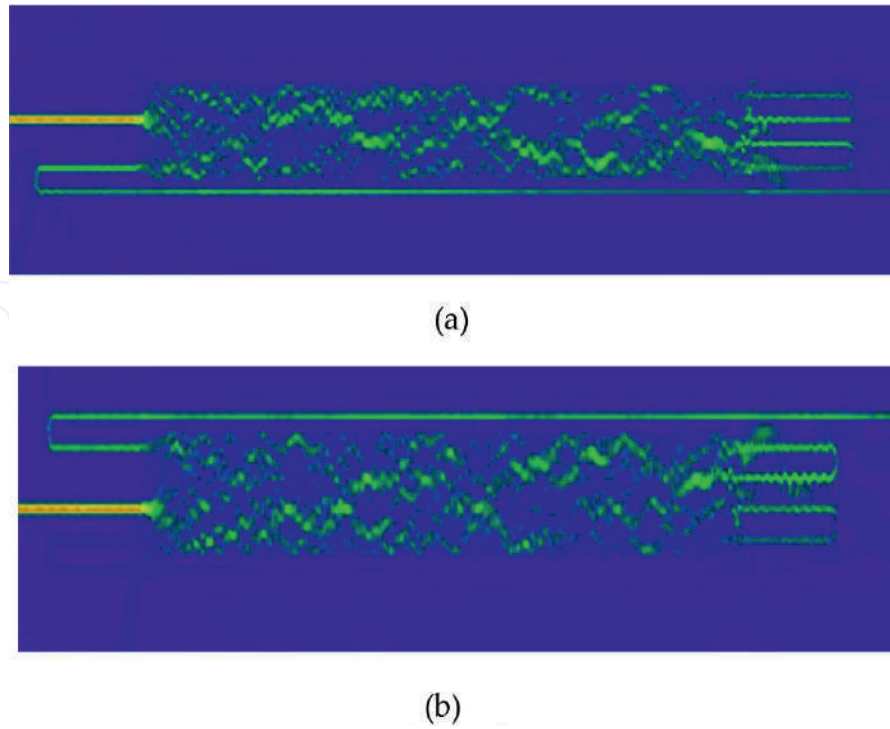**Figure 11.** MZI cell based on 4×4 MMI coupler.

Figure 12. Normalized output powers at output port 1 and 4 of a 4×4 MMI coupler.

By some calculations, the MZI cell based on 4×4 MMI coupler can be expressed by a characterized matrix

$$\mathbf{S} = \frac{1}{\sqrt{2}} \begin{bmatrix} 1 & j \\ j & 1 \end{bmatrix} \begin{bmatrix} e^{j\Delta\varphi} & 0 \\ 0 & 1 \end{bmatrix} \frac{1}{\sqrt{2}} \begin{bmatrix} 1 & j \\ j & 1 \end{bmatrix} = e^{j\frac{\Delta\varphi}{2}} \begin{bmatrix} \tau & \kappa \\ \kappa^* & -\tau^* \end{bmatrix} \tag{10}$$

Figure 13. Optical field propagation through the coupler for input signal presented at port 2 and 3.

where $\tau = \sin\left(\frac{\Delta\varphi}{2}\right)$, and $\kappa = \cos\left(\frac{\Delta\varphi}{2}\right)$.

Finally, we use finite difference time difference (FDTD) method to simulate the proposed MZI cell and then make a comparison with the analytical theory. The proposed MZI cell has two feedback waveguides. Although the BPM has an advantage of fast simulations and it is widely used technique to simulate light propagation in slowly varying non-uniform guiding structures, it is not suitable for simulating the proposed MZI structure. The FDTD has a disadvantage of a time-consuming simulation, and it has very accurate results. In our FDTD simulations, we take into account the wavelength dispersion of the silicon waveguide. A light pulse of 15 fs pulse width is launched from the input to investigate the transmission characteristics of the device. The grid sizes $\Delta x = \Delta y = \Delta z = 20$ nm are chosen in our simulations for accurate simulations [34]. The FDTD simulations for the MZI cell are shown in **Figure 13**. The simulations show that the device operation has a good agreement with our prediction by analytical theory.

5. Waveguide mesh design with new MZI cell

The new proposed MZI cell is a basic building block for mesh design to produce new functional devices for photonic applications. For example, by using the hexagonal mesh shown in
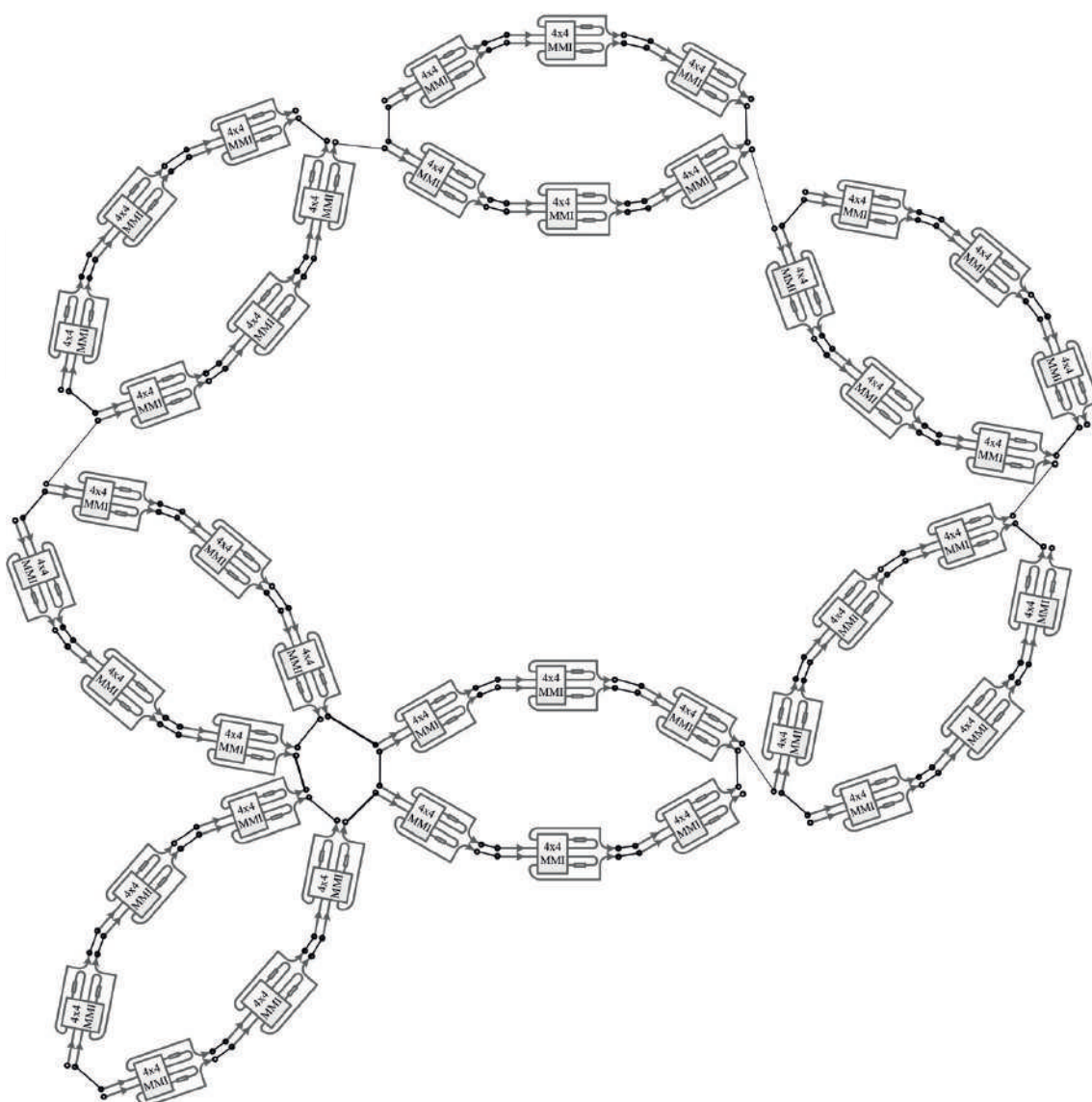
Figure 14. Reconfigurable mesh design based on new MZI cell.

Figure 14, optical filters and switches can be achieved by properly controlling the phase shifters.

6. Conclusions

We presented a new compact MZI cell based on silicon on insulator waveguides. The structure requires only one 4×4 multimode interference coupler. The PN junction waveguide is used to achieve reconfigurable devices. The device operation has been verified by using the FDTD. This MZI cell can be useful for complex mesh designs applied to optical applications.

Author details

Trung-Thanh Le

Address all correspondence to: thanh.le@vnu.edu.vn

International School (VNU-IS), Vietnam National University (VNU), Hanoi, Vietnam

References

[1] Agrawal GP. Fiber Optic Communication Systems. New York: John Wiley & Sons; 2002

[2] Le T-T, Cahill L. Microresonators based on 3 × 3 restricted interference MMI couplers on an SOI platform. In: IEEE LEOS Annual Meeting Conference Proceedings (LEOS 2009). Belek-Antalya, Turkey; October 4–8, 2009. pp. 479-480

[3] Le T-T, Cahill L. The design of 4 × 4 multimode interference coupler based microring resonators on an SOI platform. Journal of Telecommunications and Information Technology. 2009;**2**:98-102

[4] Le TT, Cahill LW. The design of wavelength selective switches and filters based on SOI microring resonators. In: 2007 Asia-Pacific Conference on Communications; 2007. pp. 3-5

[5] Le D-T, Nguyen N-M, Le T-T. Development of PAM-4 signaling for high performance computing, supercomputers and data center systems. Journal of Science and Technology on Information and Communications. 2017;**1**:34-38

[6] Le T-T. Realization of a multichannel chemical and biological sensor using 6 × 6 multimode interference structures. International Journal of Information and Electronics Engineering. 2011;**2**:240-244

[7] Le T-T. Microring resonator based on 3 × 3 general multimode interference structures using silicon waveguides for highly sensitive sensing and optical communication applications. International Journal of Applied Science and Engineering. 2013;**11**:31-39

[8] Le T-T. Two-channel highly sensitive sensors based on 4 × 4 multimode interference couplers. Photonic Sensors. 2017;**7**:357-364, 2017/12/01

[9] Le TT, Cahill LW, Elton DM. Design of 2 × 2 SOI MMI couplers with arbitrary power coupling ratios. Electronics Letters. 2009;**45**:1118-1119

[10] Le T-T. Arbitrary power splitting couplers based on 3 × 3 multimode interference structures for all-optical computing. International Journal of Engineering and Technology. 2011;**2**:565-569

[11] Le T-T. Realization of all-optical type i discrete cosine and sine transforms using multimode interference structures. International Journal of Microwave and Optical Technology (IJMOT). 2012;**7**:127-134

[12] Le T-T. All-optical Karhunen–Loeve transform using multimode interference structures on silicon nanowires. Journal of Optical Communications. 2011;**32**:217-220

[13] Le T-T. The design of optical signal transforms based on planar waveguides on a silicon on insulator platform. International Journal of Engineering and Technology. 2010;**2**:245-251

[14] Le T-T. Arbitrary power splitting couplers based on 3×3 multimode interference structures for all-optical computing. International Journal of Engineering and Technology. 2011;**3**:565-569

[15] Le D-T, Le T-T. Coupled resonator induced transparency (CRIT) based on interference effect in 4×4 MMI coupler. International Journal of Computer Systems (IJCS). 2017;**4**:95-98

[16] Le T-T. Multimode Interference Structures for Photonic Signal Processing. Germany: LAP Lambert Academic Publishing; 2010

[17] Cahill LW, Le TT. MMI devices for photonic signal processing. In: 9th International Conference on Transparent Optical Networks (ICTON 2007). Rome, Italy; July 1–5, 2007. pp. 202-205

[18] Cahill LW, Le TT. Photonic signal processing using MMI elements. In: 10th International Conference on Transparent Optical Networks (ICTON 2008); Athens, Greece; 22-26 June 2008. pp.114-117

[19] Le TT, Cahill LW. The modeling of MMI structures for signal processing applications. In: Greiner CM, Waechter CA, editors. Integrated Optics: Devices, Materials, and Technologies XII. Proceedings of the SPIE. Vol. 6896. San Jose, California, United States: Society of Photo-Optical Instrumentation Engineers (SPIE); pp. 68961G-68961G-7, 03/2008

[20] Le TT, Cahill L. All-optical signal processing circuits using silicon waveguides. In: The 7th International Conference on Broadband Communications and Biomedical Applications. Melbourne, Australia; ; November 21–24, 2011. pp. 167-172

[21] Carolan J, Harrold C, Sparrow C, et al. Universal linear optics. Science. 2015;**349**:711

[22] Miller DAB. Self-aligning universal beam coupler. Optics Express. 2013;**21**:6360-6370

[23] Reck M, Zeilinger A, Bernstein HJ, et al. Experimental realization of any discrete unitary operator. Physical Review Letters. 1994;**73**:58-61

[24] Shen Y, Harris NC, Skirlo S, et al. Deep learning with coherent nanophotonic circuits. Nature Photonics. 2017;**11**:441

[25] Perez D, Gasulla I, Fraile FJ, et al. Silicon photonics rectangular universal interferometer. Laser & Photonics Reviews. 2017;**11**:1700219

[26] Xia F, Sekaric L, Vlasov YA. Mode conversion losses in silicon-on-insulator photonic wire based racetrack resonators. Optics Express. 2006;**14**:3872-3886

[27] Baehr-Jones T, Ding R, Liu Y, et al. Ultralow drive voltage silicon traveling-wave modulator. Optics Express. 2012;**20**:12014-12020

[28] Emelett SJ, Soref R. Design and simulation of silicon microring optical routing switches. IEEE Journal of Lightwave Technology. 2005;**23**:1800-1808

[29] Heebner J, Grover R, Ibrahim T. Optical Microresonators: Theory, Fabrication, and Applications. London: Springer; 2008

[30] Le T-T, Cahill L. Generation of two Fano resonances using 4×4 multimode interference structures on silicon waveguides. Optics Communications. 2013;**301-302**:100-105

[31] Bachmann M, Besse PA, Melchior H. General self-imaging properties in $N \times N$ multimode interference couplers including phase relations. Applied Optics. 1994;**33**:3905

[32] Soldano LB, Pennings ECM. Optical multi-mode interference devices based on self-imaging: Principles and applications. IEEE Journal of Lightwave Technology. 1995;**13**:615-627

[33] Le T-T. An improved effective index method for planar multimode waveguide design on an silicon-on-insulator (SOI) platform. Optica Applicata. 2013;**43**:271-277

[34] Le D-T, Nguyen M-C, Le T-T. Fast and slow light enhancement using cascaded microring resonators with the Sagnac reflector. Optik – International Journal for Light and Electron Optics. 2017;**131**:292-301